

AN AROMATIC INVENTORY OF THE LOCAL VOLUME

A. R. MARBLE¹, C. W. ENGELBRACHT¹, L. VAN ZEE², D. A. DALE³, J. D. T. SMITH⁴, K. D. GORDON⁵, Y. WU⁶, J. C. LEE⁷,
R. C. KENNICUTT⁸, E. D. SKILLMAN⁹, L. C. JOHNSON¹⁰, M. BLOCK¹, D. CALZETTI¹¹, S. A. COHEN³, H. LEE¹², M. D. SCHUSTER³

ABSTRACT

Using infrared photometry from the *Spitzer Space Telescope*, we perform the first inventory of aromatic feature emission (AFE, but also commonly referred to as PAH emission) for a statistically complete sample of star-forming galaxies in the local volume. The photometric methodology involved is calibrated and demonstrated to recover the aromatic fraction of the IRAC $8\mu\text{m}$ flux with a standard deviation of 6% for a training set of 40 SINGS galaxies (ranging from stellar to dust dominated) with both suitable mid-infrared *Spitzer* IRS spectra and equivalent photometry. A potential factor of two improvement could be realized with suitable $5.5\mu\text{m}$ and $10\mu\text{m}$ photometry, such as what may be provided in the future by *JWST*. The resulting technique is then applied to mid-infrared photometry for the 258 galaxies from the Local Volume Legacy (LVL) survey, a large sample dominated in number by low-luminosity dwarf galaxies for which obtaining comparable mid-infrared spectroscopy is not feasible. We find the total LVL luminosity due to five strong aromatic features in the $8\mu\text{m}$ complex to be $2.47 \times 10^{10} L_{\odot}$ with a mean volume density of $8.8 \times 10^6 L_{\odot} \text{Mpc}^{-3}$. Twenty-four of the LVL galaxies, corresponding to a luminosity cut at $M_B = -18.22$, account for 90% of the aromatic luminosity. Using oxygen abundances compiled from the literature for 129 of the 258 LVL galaxies, we find a correlation between metallicity and the aromatic to total infrared emission ratio but not the aromatic to total $8\mu\text{m}$ dust emission ratio. A possible explanation is that metallicity plays a role in the abundance of aromatic molecules relative to the total dust content, but other factors such as star formation and/or the local radiation field affect the excitation of those molecules.

Subject headings: galaxies: ISM — infrared: galaxies — surveys — techniques: photometric

1. INTRODUCTION

It is well established that the infrared spectra of galaxies tend to be dominated by emission from dust (see, e.g., the review by Rieke & Lebofsky 1979). This light is a significant fraction of the bolometric emission from galaxies, making up roughly half the extragalactic background luminosity (e.g., Lagache et al. 2005). Investigation into the composition of the responsible dust grains is hindered by the small number of known associated emission and absorption lines. The strongest features, by far, are a set of emission bands in the $3 - 17\mu\text{m}$ range that are commonly observed in galaxies. In luminous galaxies where the mid-infrared emission is dominated by star formation, they appear to be ubiquitous (Roche et al. 1991) with little (Lu et al. 2003), but not negligible (Smith et al. 2007b), relative variation in feature strength.

These features have been referred to as the mid-infrared emission bands, the unidentified infrared bands, aromatic emission features, and variations thereof. They have been tentatively identified as arising from polycyclic aromatic hydrocarbons (PAHs; Leger & Puget 1984) and are often cited as resulting from a mixture of such particles. Regardless of the exact composition, it is widely agreed that the features in question arise from various bending and stretching modes of aromatic molecules largely composed of carbon and hydrogen; therefore, we refer to the resultant emission simply as aromatic emission or aromatic feature emission (AFE).

While present in nearly all star formation dominated galaxies, aromatic features do exhibit some dependence on galaxy host properties. It has been known for years that they can be weaker, or absent altogether, in systems characterized by low metallicity and high star formation intensity (Roche et al. 1991; Thuan et al. 1999). Madden (2000) suggested that metallicity might be an important parameter, and this was shown to be true using the *Spitzer Space Telescope* (Werner et al. 2004) by Engelbracht et al. (2005) and others (Wu et al. 2006; Jackson et al. 2006; Rosenberg et al. 2008) and by detailed examination of data from the *Infrared Space Observatory* (ISO; Madden et al. 2006). Further, the weakening of aromatic features in the low-metallicity outskirts of the galaxy M101 was attributed by Gordon et al. (2008) to the hardness of the radiation field, which was also suggested to be a factor by the work of Madden et al. (2006) and Engelbracht et al. (2008).

Investigations of mid-infrared aromatic feature emission are generally based on spectroscopic observations made from above the Earth's atmosphere; for example, with *Spitzer's* Infrared Spectrograph (IRS; Houck et al. 2004b). As such, they are largely relegated to samples of galaxies that are relatively small and/or bright. Taking advantage of the fact

¹ Steward Observatory, University of Arizona, Tucson, AZ 85721 USA

² Department of Astronomy, Indiana University, Bloomington, IN 47405 USA

³ Department of Physics and Astronomy, University of Wyoming, Laramie, WY 82071 USA

⁴ Ritter Astrophysical Research Center, University of Toledo, Toledo, OH 43603

⁵ Space Telescope Science Institute, Baltimore, MD 21218 USA

⁶ Infrared Processing and Analysis Center, California Institute of Technology, Pasadena, CA 91125 USA

⁷ Carnegie Observatories, Pasadena, CA 91101 USA

⁸ Institute of Astronomy, University of Cambridge, Cambridge CB3 0HA, UK

⁹ Astronomy Department, University of Minnesota, Minneapolis, MN 55455 USA

¹⁰ Department of Astronomy, University of Washington, Seattle, WA 98195 USA

¹¹ Astronomy Department, University of Massachusetts, Amherst, MA 01003 USA

¹² Gemini Observatory, Southern Operations Center, Casilla 603, La Serena, Chile

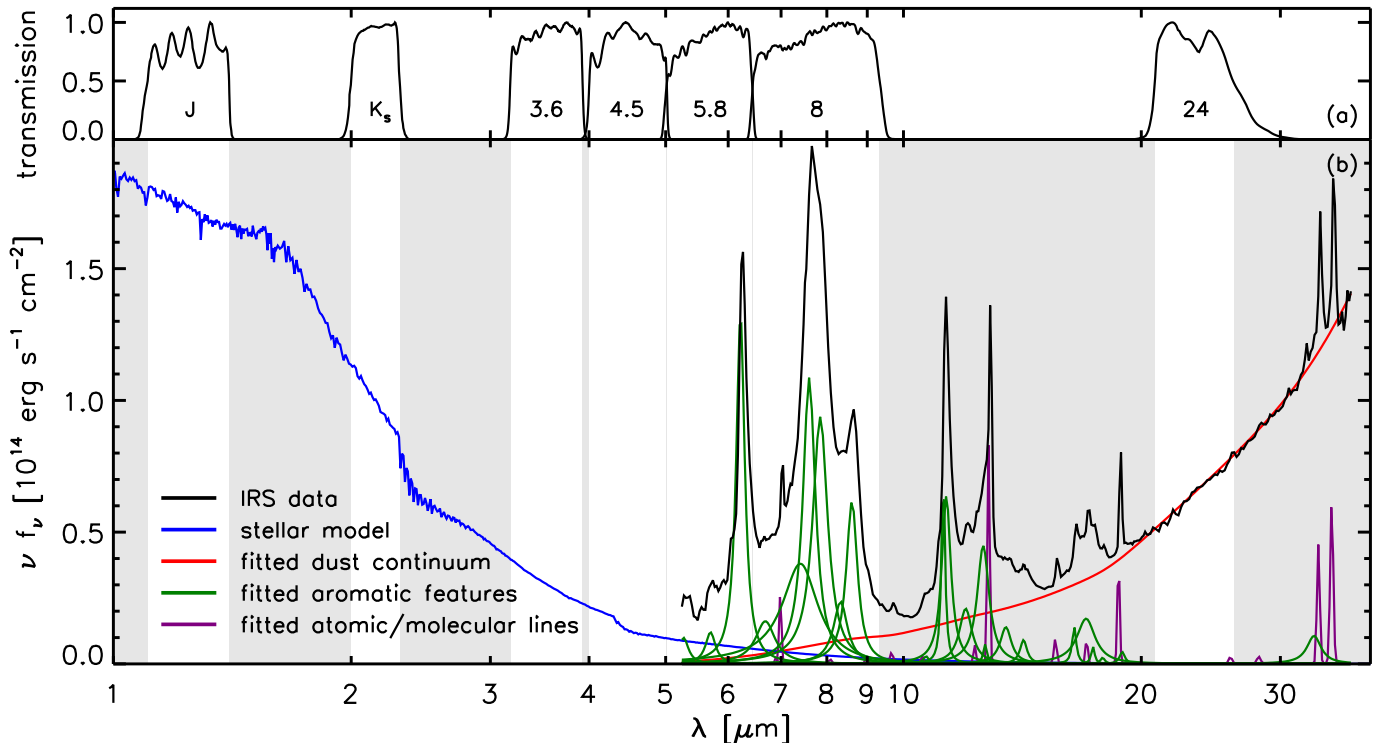


FIG. 1.— (a) Spectral response of the J , K_s , IRAC 3.6/4.5/5.8/8.0 μm , and MIPS 24 μm broad bands (the lighter regions below indicate wavelength ranges where the response is greater than half of the maximum). (b) IRS spectrum of NGC 4536 (solid black line) and its constituent flux contributions. The stellar model (blue) is an interpolation of the 100 Myr Starburst99 SEDs (for the metallicity of NGC 4536), extinction-corrected and scaled to match the $J-K_s$ color and 3.6 μm flux of NGC 4536. The aromatic features (green), atomic/molecular lines (purple), and dust continuum (red) were simultaneously fit using PAHFIT.

that several of the strongest features fall within the rest-frame 8 μm band (see Figure 1) of the Infrared Array Camera (IRAC; Fazio et al. 2004) on *Spitzer*, Engelbracht et al. (2005, 2008) introduced a purely photometric approach to measuring the strengths of aromatic features. However, the agreement between photometrically and spectroscopically determined AFE equivalent widths for 27 starburst galaxies in Engelbracht et al. (2008) was characterized by a Spearman rank-order correlation coefficient of only $r_s = 0.46$.

In this paper, we refine the photometric prescription for measuring aromatic feature emission at 8 μm , demonstrate its improved reliability, and apply it to the statistically complete sample of 258 local star-forming galaxies comprising the Local Volume Legacy survey (LVL; Dale et al. 2009). By doing so, we hope to advance future AFE investigations with a larger, more diverse, and less biased data set. In § 2, we introduce the LVL galaxies as well as an additional spectroscopic sample used for diagnostic purposes. The corresponding datasets are described in § 3, while in § 4 our methodology is detailed and tested. Finally, we present an inventory of LVL aromatic feature emission measurements as well as a brief characterization of them in § 5 before summarizing our findings in § 6.

2. GALAXIES

The *Spitzer Space Telescope* Local Volume Legacy is a two-tiered survey of a statistically complete sample of nearby star-forming galaxies. The inner tier includes all known galaxies within 3.5 Mpc that lie outside the Local Group and the galactic plane ($|b| > 20^\circ$), as well as those galaxies in the M81 group and the Sculptor filament. The outer tier is comprised of all galaxies brighter than $m_B < 15.5$ that lie within

11 Mpc and have $|b| > 30^\circ$. The resulting 258 galaxies are primarily those of the ACS Nearby Galaxy Survey Treasury (ANGST; Dalcanton et al. 2009) and the 11 Mpc H α and Ultraviolet Galaxy Survey (11HUGS; Kennicutt et al. 2008; Lee et al. 2009); however, a more detailed accounting can be found in Dale et al. (2009). The nearly volume-limited nature of LVL means that it is dominated in number by traditionally underrepresented low-luminosity dwarf galaxies, while the volume itself is sufficiently large to ensure a diverse cross-section of star formation properties and morphologies.

Overlapping with the 258 LVL galaxies are 40 SINGS (Kennicutt et al. 2003b) galaxies with suitable mid-infrared spectroscopy for testing and calibrating the photometric techniques applied in this paper. The combined total of 283 nearby galaxies addressed in this study is listed in Table 1 by name and celestial coordinates, along with their redshifts, distances, oxygen abundances compiled from the literature (see § 3.2), and inclusion in the LVL and/or spectroscopic subsamples. Additional properties of the LVL and SINGS galaxies which are not directly relevant to this body of work can be found in Dale et al. (2009) and Kennicutt et al. (2003b), respectively.

3. DATASETS

3.1. LVL Photometry

Our analysis of aromatic emission in the LVL galaxies draws upon global broadband photometry in the J (1.25 μm) and K_s (2.17 μm) bands, the four *Spitzer* IRAC bands (3.6, 4.5, 5.8, and 8.0 μm) and the three *Spitzer* MIPS bands (24, 70, and 160 μm). These data are presented in the prior LVL survey description and infrared photometry paper (Dale et al. 2009), where a detailed account is given of what is summarized here.

IRAC and MIPS observations were taken in two epochs at different rotations in order to remove foreground asteroids and mitigate detector artifacts. The total effective exposure time is 240 seconds for the IRAC bands and 160, 80, and 16 seconds at 24, 70, and 160 μm , respectively. For the brighter targets, additional 1.2 second IRAC images were used to recover pixels that were either saturated or in the non-linear regime. Foreground stars and background galaxies were removed from the images before photometry was extracted using the same elliptical aperture (chosen to include all detectable light) for each band. The final flux densities are corrected for Galactic extinction (Schlegel et al. 1998) assuming $A_V/E(B-V) \approx 3.1$ and the reddening curve of Li & Draine (2001), and include extended source aperture corrections but no color corrections (which are on the order of a few percent, but are not relevant for this study; see § 4.2). The J and K_s band photometry was similarly extracted from Two Micron All Sky Survey (2MASS; Skrutskie et al. 2006) images using the same apertures and masking.

Nearly all of the LVL galaxies are detected in all seven *Spitzer* bands down to $m_B \approx 14$ mag and $M_B \approx -13$ mag. Where fainter galaxies were not detected, 5σ upper limits are provided. This is the case for 59 galaxies in at least one band and nine galaxies in all nine infrared bands. Individual photometry is not provided for MCG -05-13-004, but is instead included with that of NGC 1800, as the two spatially overlap. In addition, IC 5152 was not observed at 3.6 μm or 5.8 μm , J/K_s photometry is not available for the LMC, and 5.8 $\mu\text{m}/J/K_s$ data is not included for the SMC.

3.2. LVL Oxygen Abundances

One of the expected key parameters for the formation and abundance of aromatic molecules is the metallicity of the interstellar medium. Thus, we have compiled oxygen abundances from the literature (Table 1), where measurements were available for 129 of the 258 LVL galaxies. Unless otherwise noted, all abundances are as given by the original source. When multiple sources exist, the listed abundance is the one expected to be most representative of the metallicity throughout the star-forming disk. Specifically, for low mass galaxies, where oxygen abundance gradients are negligible (e.g., Kobulnicky & Skillman 1996, 1997; van Zee & Haynes 2006), an average of high signal-to-noise ratio observations was adopted if multiple observations were available. For high mass galaxies, where abundance gradients can be substantial (e.g., Zaritsky et al. 1994), we adopt either the value from an integrated spectrum or the rough equivalent at $0.4R_{25}$.

Of particular concern for oxygen abundance compilations is the wide range of empirical strong-line abundance calibrations available in the literature. Systematic differences in empirical calibrations can result in abundance discrepancies of as much as 0.7 dex (see, e.g., the extensive discussion in Kewley & Ellison 2008). While the oxygen abundances tabulated in Table 1 have not been corrected for such systematic effects, the majority are on similar calibration scales with potential offsets of only 0.1 to 0.2 dex between sources (e.g., McGaugh 1991; Zaritsky et al. 1994). One further complication for empirical estimates of the oxygen abundance is the double valued nature of the strong-line abundance indicators (e.g., R23). We revise the oxygen abundance for UGC 04787, NGC 3510, UGC 06900, NGC 4248, and UGC 07699 based on published line strengths and the assumption that they are likely low metallicity systems, rather than high metallicity as published in the original source. Finally, we tabulate the oxy-

gen abundances published for KDG 61 and UGC 05336, but choose not to include them in our analysis (see § 5.2.3) as it is not clear that these measurements are indicative of their ISM (Croxall et al. 2009).

3.3. SINGS Spectroscopy

The galaxies comprising the spectroscopic sample were all spectrally mapped with *Spitzer's* Infrared Spectrograph (IRS; Houck et al. 2004b) as part of the SINGS survey. Full observational details regarding this spectral mapping are provided in Kennicutt et al. (2003b), while the final one-dimensional spectra are presented in Smith et al. (2007b). In brief, the latter span the wavelength range 5–38 μm with spectral resolution $R \approx 60-125$ and correspond to extraction apertures (provided in Table 1 of Smith et al. (2007b)) that were chosen to include the largest useful region of circumnuclear and inner disk emission (approximately the inner kiloparsec).

The spectra are comprised of data from the four low-resolution orders of IRS (SL2: 5.25–7.6 μm , SL1: 7.5–14.5 μm , LL2: 14.5–20.75 μm , LL1: 20.5–38.5 μm) which were matched in the overlap regions in such a way that preserves the flux calibration of the LL2 segment. However, for the purposes of this study, they have been normalized (with scale factors on the order of unity) to identically agree with the IRS aperture matched IRAC 8 μm flux density as described below in § 3.5. The resulting spectra are shown in Figure 2, with their statistical uncertainties shaded. However, as noted in Smith et al. (2007b), at signal-to-noise greater than approximately 10, systematic errors exceed the statistical uncertainties in some regions. Therefore, throughout our analysis, we adopt uncertainties that floor the signal-to-noise at 10.

3.4. Synthetic 2MASS/Spitzer Photometry

At various stages, our analysis employs synthetic photometry derived from either observed or modeled spectra. Here, “synthetic” refers to photometry that *would* have been obtained if a source with a spectral energy distribution given by the spectrum in question had been imaged. Essentially, this amounts to a convolution of the spectrum with the appropriate response function for the desired photometric imager/band. In the case of 2MASS J and K_s , relative spectral response curves in the appropriate units to be integrated directly over f_λ spectra are provided by Cohen et al. (2003). A few more steps are involved in calculating synthetic photometry for the IRAC and MIPS bands; however, this has been automated in the IDL routine SPITZER_SYNTHPHOT which is available from the *Spitzer* Science Center.

3.5. SINGS IRS Aperture Matched Photometry

Our purpose for the spectroscopic sample is to compare measurements derived from photometry with those obtained directly from spectroscopy. In order to ensure meaningful comparisons, the IRAC and MIPS 24 μm SINGS photometry for the spectroscopic sample was extracted with apertures matched to the IRS data. Aside from this, an improved background subtraction algorithm, and the aperture corrections described in Smith et al. (2007a), it corresponds to the global photometry detailed in Dale et al. (2007), which closely resembles the LVL photometry in its observational details and data reduction.

Any residual calibration differences between the SINGS spectroscopy and photometry were removed by scaling the IRS spectra such that synthetic 8 μm photometry identically

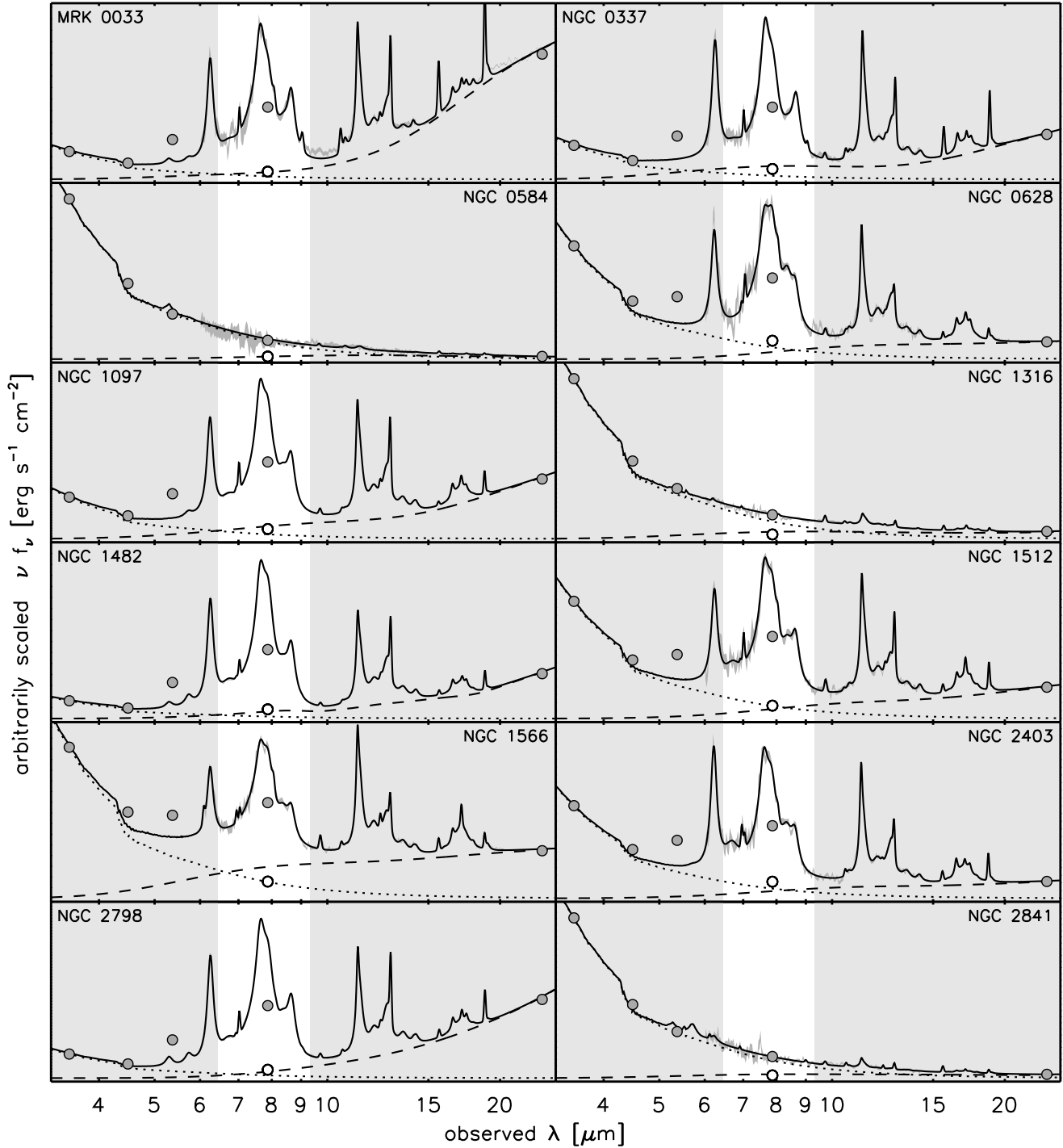


FIG. 2.— *Spitzer* IRS spectra (solid line) with aperture matched IRAC photometry and synthetic MIPS $24\mu\text{m}$ photometry (filled circles) for the spectroscopic sample. The unshaded portion of the logarithmic wavelength axis corresponds to the coverage of the IRAC $8\mu\text{m}$ band. The $1\text{-}\sigma$ envelope of the *statistical* uncertainty in the IRS spectra is also shaded. The modelled stellar and fitted (using PAHFIT) dust continuum contributions are shown as dotted and dashed lines, respectively. The latter can be compared to the photometrically derived value (empty circle) given by Equations (5)–(7).

reproduced the aperture matched IRAC $8\mu\text{m}$ flux density. This introduces greater uncertainty than normalization to the MIPS $24\mu\text{m}$ flux density, and would be inadvisable if absolute measurements of AFE were our primary concern. Since we are instead motivated by minimizing relative differences between the spectroscopic and photometric values, it is to our advantage to scale the IRS spectra to match the site of the aromatic feature complex of interest. Furthermore, synthetic $24\mu\text{m}$ photometry was obtained directly from the scaled spec-

tra, in lieu of the aperture matched MIPS values. The rms of the corresponding relative difference is approximately 10%, which we universally adopt as the uncertainty in the broadband photometry used for the spectroscopic sample (provided in Table 2).

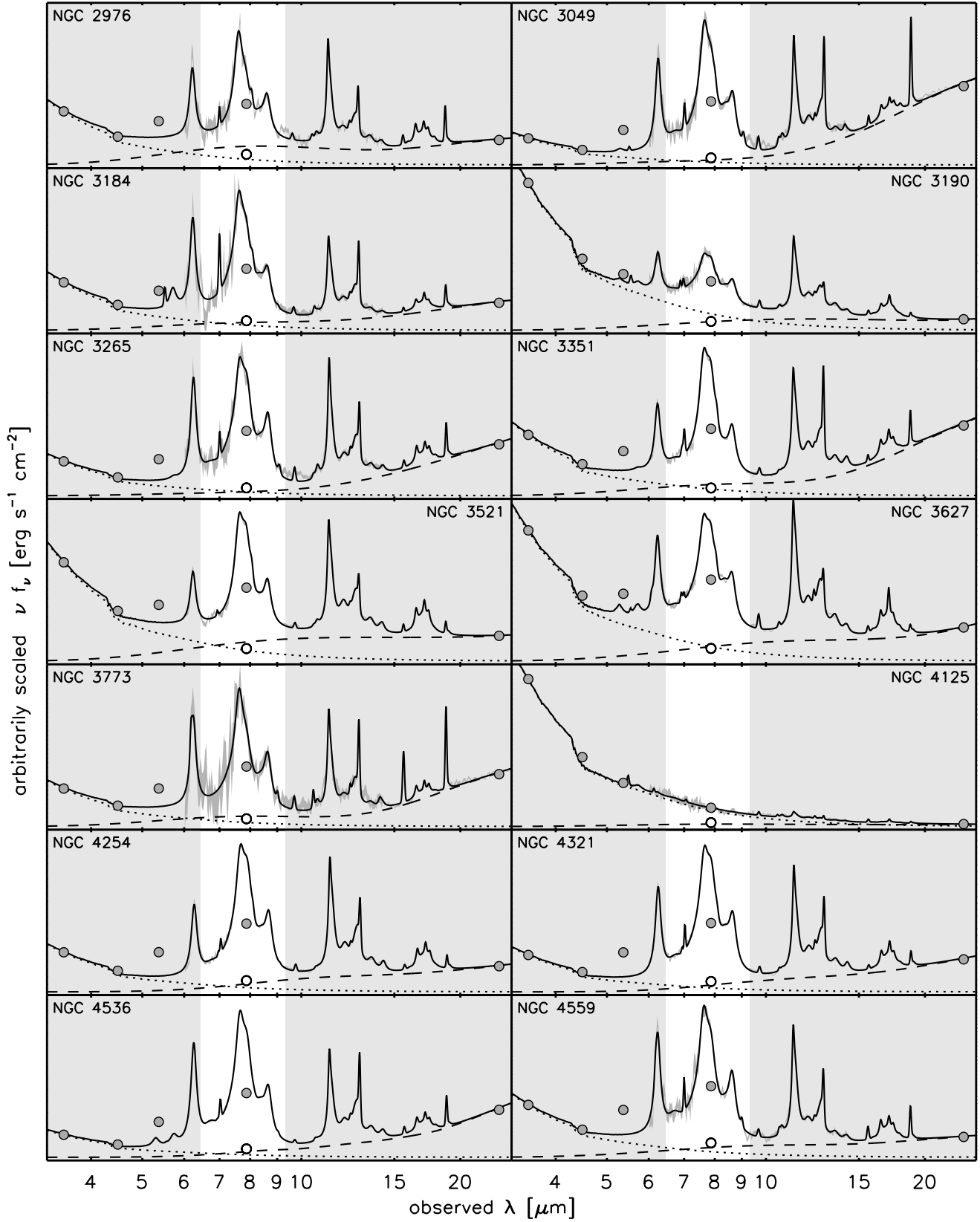


FIG. 2.—Continued

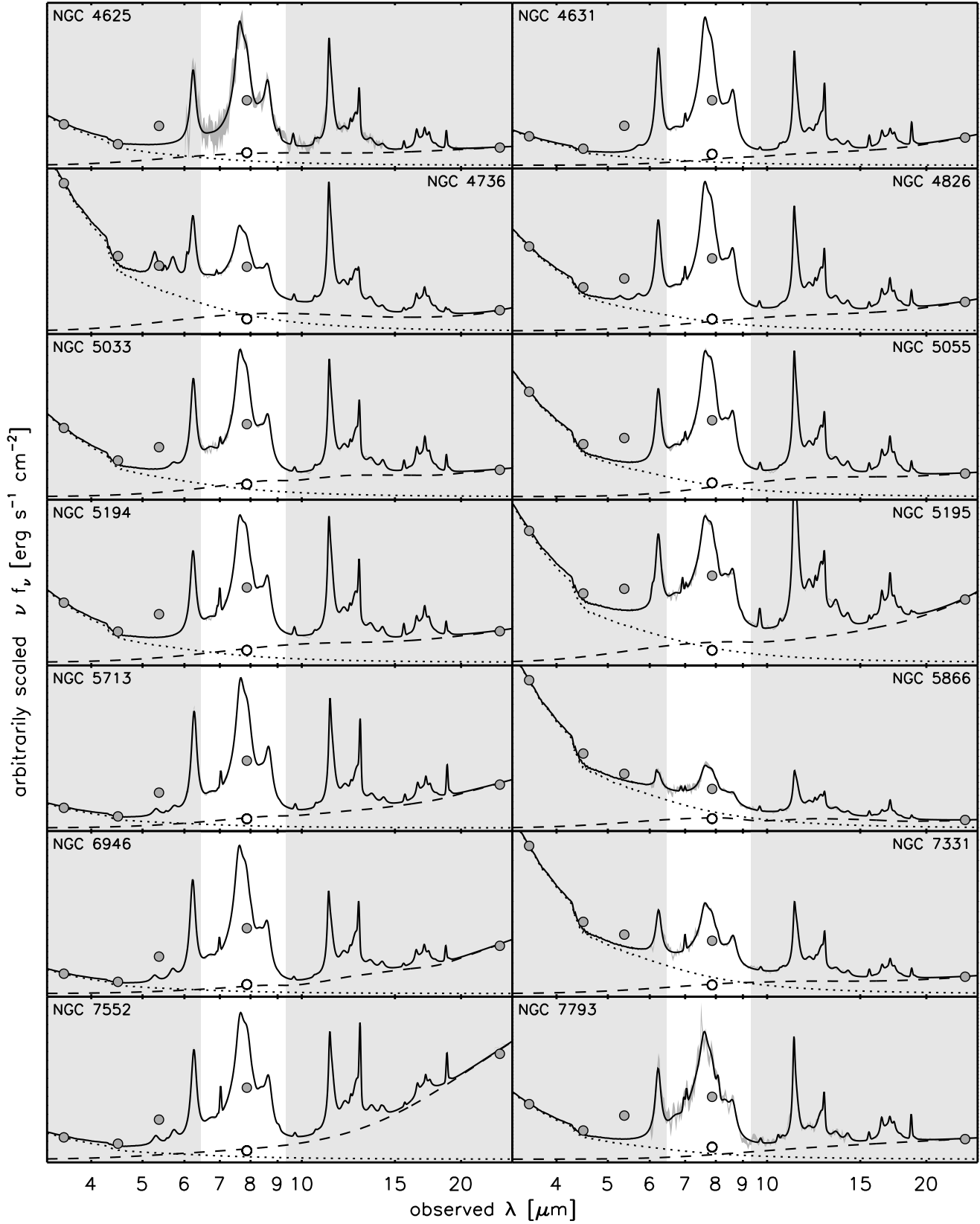


FIG. 2.—Continued

4. METHODOLOGY

4.1. LVL L-Z Relationship

The LVL oxygen abundances compiled from the literature (see § 3.2) exhibit the well known luminosity-metallicity (L-Z) correlation with stellar luminosity (Figure 3). Weighted by the statistical $1\text{-}\sigma$ uncertainties for both parameters, the best linear fit is given by

$$12 + \log(\text{O}/\text{H}) = 5.06 \pm 0.04 - (0.164 \pm 0.002) M_{4.5}, \quad (1)$$

which agrees reasonably well with previous results for other samples (e.g., Lee et al. 2006). The scatter in oxygen abundance with respect to the linear fit is generally consistent with the statistical uncertainties plus an additional approximately 0.15 dex systematic calibration error. A few outliers (e.g., UGC 05340 and NGC 4656) may also be affected by errors in distance measurements. Subsequently, we adopt the oxygen abundance given by Equation (1) for galaxies without measurements in the literature. However, these L-Z based abundances are used only for the purpose of applying metallicity corrections to stellar SED models (§ 4.2.1).

4.2. AFE Measurement

The rest-frame mid-infrared portion of a galaxy’s spectral energy distribution is typically a combination of aromatic features, atomic and molecular lines, and continua of dust emission and starlight. As demonstrated by Smith et al. (2007b) and illustrated in Figure 1, these components can be simultaneously fitted given a spectrum of sufficient resolution and signal-to-noise. One measure of the strength of the aromatic emission, $F_{8(S)}^{\text{afe}}$, is then given by integrating and summing the flux in the $8\mu\text{m}$ complex formed by individual features at 7.42, 7.60, 7.85, 8.33, and 8.61 μm .

However, this complex conveniently falls within the broad IRAC $8\mu\text{m}$ band, providing an alternative means for mea-

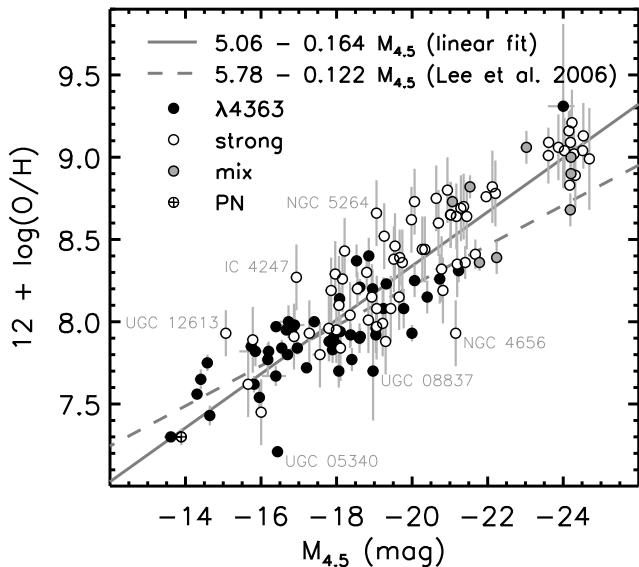


FIG. 3.— Oxygen abundance versus IRAC $4.5\mu\text{m}$ absolute magnitude for 127 LVL galaxies. Weighted by the statistical $1\text{-}\sigma$ uncertainties shown for both parameters, the corresponding luminosity-metallicity relationship has a $5.06 \pm 0.04 - (0.164 \pm 0.002) M_{4.5}$ linear fit (solid line) that is marginally consistent with the $5.78 \pm 0.21 - (0.122 \pm 0.012) M_{4.5}$ dashed line reported by Lee et al. (2006). Note that some of the scatter (a few outliers are labeled) is due to a *systematic* uncertainty of 0.1–0.2 for the inhomogeneous oxygen abundance measurements drawn from the literature.

suring the strength of the aromatic features if their contribution can be disentangled from the total flux. For the spectroscopic sample, 3–96 (with a mean of 19) percent of this total comes from starlight, while the dust continuum is responsible for 6–32 (with a mean of 16) percent of the non-stellar emission. Combined, the two continuum sources contribute 12–100 (with a mean of 34) percent of the IRAC $8\mu\text{m}$ flux density. We build upon earlier work by Engelbracht et al. (2005, 2008), exploiting our spectroscopic galaxy sample to motivate, calibrate, and test a purely photometric determination of aromatic emission at $8\mu\text{m}$, $F_{8(S)}^{\text{afe}}$. For clarity, spectroscopically derived values are distinguished from their photometrically based counterparts by a parenthetical letter S in the subscript (e.g., $F_{8(S)}^{\text{afe}}$).

4.2.1. Starlight

The same determination of the stellar contribution to the mid-infrared is utilized for both the spectroscopic and photometric analyses; therefore, we address it separately and first. The stellar continuum is the tail of a distribution that peaks in the optical or near-infrared, which, like Engelbracht et al. (2008), we model using SEDs generated by the stellar population synthesis code Starburst99 and described in Leitherer et al. (1999) and Vázquez & Leitherer (2005). These are available for a range of ages between one Myr and one Gyr and for metallicities $Z = 0.040, 0.020, 0.008, 0.004,$ and 0.001 , or $12 + \log(\text{O}/\text{H}) = 7.6, 8.2, 8.5, 8.9,$ and 9.2 given the Starburst99 assumed solar values of $Z_{\odot} = 0.02$ and $12 + \log(\text{O}/\text{H})_{\odot} = 8.9$.

As confirmed by Engelbracht et al. (2008), changes in the stellar continuum slope for these instantaneous star formation models are insignificant in the IRAC bands beyond 5–15 Myr; therefore, we arbitrarily adopt an age of 100 Myr. The corresponding set of SEDs are redshifted and interpolated to match either the observed velocity and oxygen abundance listed in Table 1 or, if unavailable, the values approximated by the Hubble relation ($v_{\text{km/s}} = 72 D_{\text{Mpc}}$) and Equation (1). The resulting spectrum is adjusted for internal extinction, assuming the extinction law of Rieke & Lebofsky (1985) and a simple foreground screen, by multiplying it with $10^{-0.1516 A_V \lambda^{-1.475}}$, where A_V is equal to $16.04 (\log(f_{\text{J}}^{\text{sb99}}/f_{\text{K}_s}^{\text{sb99}}) - \log(f_{\text{J}}^{\text{obs}}/f_{\text{K}_s}^{\text{obs}}))$, f^{sb99} corresponds to synthetic photometry from the stellar spectrum, and f^{obs} is the observed photometry for the galaxy in question. In the case of 39 LVL galaxies, $f_{\text{J}}^{\text{sb99}}/f_{\text{K}_s}^{\text{sb99}}$ is unknown and 1.22 (the median of the remainder) is assumed. For the galaxies considered in this paper, these redshift, metallicity, and extinction corrections are a few percent or less.

Whereas Engelbracht et al. (2008) normalized their stellar SED to the mean of the observed K_s and IRAC $3.6\mu\text{m}$ band flux densities, we choose to use only the latter. This has the advantage that the absolute calibration of our methodology is tied to a single photometric system, not to mention the fact that available K_s band photometry is highly uncertain for the dwarf galaxies comprising the majority of the LVL sample. This normalization is done by scaling the stellar model such that synthetic IRAC photometry matches the observed photometry at $3.6\mu\text{m}$. Implicit here is the assumption that the IRAC $3.6\mu\text{m}$ band is a reliable tracer of global stellar emission, an assertion supported by Pahre et al. (2004) and the modelling of Draine & Li (2007). As we are not addressing starburst galaxies or those with especially hot dust, we do not

need to be concerned with contamination from a strong dust continuum or significant aromatic emission from the $3.3\mu\text{m}$ feature.

Determining the stellar component of the IRS spectra described in § 3.3 is then simply a matter of interpolating the stellar SED onto the same wavelength scale. Similarly, synthetic photometry of the stellar SED yields the stellar component of the flux density in band X (henceforth referred to as f_X^{str}). The resulting ratio of $f_X^{\text{str}}/f_{3.6}^{\text{str}}$ is approximately 58, 39, 24, and 2.8 percent, respectively, for X = 4.5, 5.7, 8, and 24 microns. Table 2 provides f_8^{str} for the spectroscopic sample, while Table 3 includes f_X^{str} for the MIPS $24\mu\text{m}$ band and all of the IRAC bands (except for $3.6\mu\text{m}$ where $f_{3.6}^{\text{str}} = f_{3.6}$). Throughout the remainder of the paper, we represent the non-stellar, or stellar-subtracted, photometry with the ^{ns} superscript,

$$f_X^{\text{ns}} = f_X - f_X^{\text{str}}. \quad (2)$$

Disregarding any error in the model or response function, the statistical uncertainty in our synthetic stellar photometry is given by appropriately scaling the uncertainty at $3.6\mu\text{m}$ flux. For the data considered in this paper, the resulting uncertainty in the stellar flux is always less than the corresponding uncertainty in the total flux. Thus, the error associated with stellar subtraction is negligible.

4.2.2. Spectroscopic Dust Decomposition

Spectroscopic aromatic feature emission measurements were obtained from the stellar-subtracted IRS spectra using the IDL program PAHFIT (Smith et al. 2007b). This spectral decomposition code simultaneously fits up to eight dust continuum components with modified blackbodies at fixed temperatures ranging from 35–300 K, 18 Gaussian atomic and molecular lines (listed in Table 2 of Smith et al. (2007b)), 25 separate aromatic features with Drude profiles (listed in Table 3 of Smith et al. (2007b)), and absorption from dust extinction in the form of a power law plus silicate features at 9.7 and 18 μm . By default, PAHFIT also fits a simple starlight component (a 5×10^3 K blackbody); however, we fixed this to be zero for our previously stellar-subtracted spectra.

In addition to the spectroscopy, the stellar-subtracted IRAC 3.6 and 4.5 μm photometry were included in the fit to extend the wavelength coverage at the blue end. The results are shown in Figure 2 and quantified in Table 2 in the form of synthetic IRAC $8\mu\text{m}$ photometry of the atomic/molecular lines ($f_{8(S)}^{\text{nl}}$), total dust continuum ($f_{8(S)}^{\text{cnt}}$), and $8\mu\text{m}$ complex of aromatic features (7.42, 7.60, 7.85, 8.33, and 8.62 μm ; $f_{8(S)}^{\text{afe}}$), as well as integrated fluxes for the $8\mu\text{m}$ complex ($F_{8(S)}^{\text{afe}}$) and the 23 aromatic features spanning the mid-infrared from 5.5 μm to 20 μm ($F_{\text{mir}(S)}^{\text{afe}}$). Synthetic IRAC $8\mu\text{m}$ photometry of the previously subtracted stellar continuum (f_8^{str}) is also provided.

4.2.3. Photometric Dust Decomposition

The photometric equivalent of the integrated flux in the $8\mu\text{m}$ complex of aromatic features is proportional to the contribution of those features to the monochromatic IRAC $8\mu\text{m}$ flux density f_8^{afe} ,

$$F_8^{\text{afe}} = c_1 10^{-23} f_8^{\text{afe}}. \quad (3)$$

The constant c_1 (to be solved for subsequently) primarily reflects the width of the IRAC $8\mu\text{m}$ transmission curve ($\Delta\nu \approx$

1.3×10^{13} Hz), but also, to first order, its departure from an idealized step function. The factor of 10^{-23} is simply for convenience, yielding units of $\text{ergs}^{-1} \text{cm}^{-2}$ for F_8^{afe} given f_8^{afe} in Janskys.

We define f_8^{afe} to be the scaled remainder of the non-stellar IRAC $8\mu\text{m}$ flux density after subtracting the contribution from the dust continuum,

$$f_8^{\text{afe}} = c_2 (f_8^{\text{ns}} - f_8^{\text{cnt}}). \quad (4)$$

The scale factor ($c_2 \lesssim 1$) generically accounts for additional aromatic features that overlap with the IRAC $8\mu\text{m}$ band and, to a much lesser degree, flux from atomic and molecular lines. Both of these contributions are indeed correlated to f_8^{afe} .

We estimate the dust continuum contribution to the IRAC $8\mu\text{m}$ band by extrapolating a power law tethered to stellar-subtracted neighboring bands. At the red end, MIPS $24\mu\text{m}$ is conveniently dominated by the dust continuum, despite being further removed from $8\mu\text{m}$ than would be ideal. Several choices for the blue end are provided by the remaining IRAC bands. The 5.8 μm band has the disadvantage of including a strong aromatic feature ($\lambda = 6.22\mu\text{m}$), whereas the 4.5 μm band can have insufficient dust continuum flux for reliable anchorage of the power law. As a compromise, we adopt the mean of the two,

$$f_8^{\text{cnt}} = c_3 \left(\frac{f_{4.5}^{\text{ns}} + f_{5.8}^{\text{ns}}}{2} \right)^{1-\alpha} f_{24}^{\text{ns} \alpha}, \quad (5)$$

where

$$\alpha = \frac{\log(\lambda_8) - \log\left(\frac{\lambda_{4.5} + \lambda_{5.8}}{2}\right)}{\log(\lambda_{24}) - \log\left(\frac{\lambda_{4.5} + \lambda_{5.8}}{2}\right)} = 0.282, \quad (6)$$

and λ_X refers to the effective wavelength of band X ($\lambda_{4.5} = 4.493\mu\text{m}$, $\lambda_{5.8} = 5.731\mu\text{m}$, $\lambda_8 = 7.872\mu\text{m}$, and $\lambda_{24} = 23.675\mu\text{m}$).

The leading coefficient c_3 is included to account for any systematic difference between our simple model and the true dust continua. A constant value of 0.594 yields the same mean for f_8^{cnt} as the synthetic $8\mu\text{m}$ photometry from the fitted dust continua; however, the success of the power law indicator in reproducing $f_{8(S)}^{\text{cnt}}$ for a given galaxy is correlated with mid-infrared color (Figure 4a), and the rms of the difference relative to the total flux is improved by adopting

$$c_3 = 0.149 + 0.516 \left(\frac{f_8}{f_{24}} \right). \quad (7)$$

With this correction applied, the rms of the relative error in f_8^{cnt} is still 0.54. However, for the purposes of measuring aromatic emission, we are primarily concerned with how well we can constrain the fraction of f_8 contributed by the dust continuum. Together, Equations (5)–(7) recover the spectroscopically determined fraction $f_{8(S)}^{\text{cnt}}/f_8$ with an rms of only 0.064 (see Figure 4b, as well as individual results included in Figure 2). While power law extrapolation is not the only means for estimating the dust continuum, other methods (e.g., spectral templates) bear little hope for producing better overall agreement if they are calibrated with the same free parameters (photometry). Future datasets including flux densities at more ideal wavelengths may improve these results or enable a more sophisticated methodology.

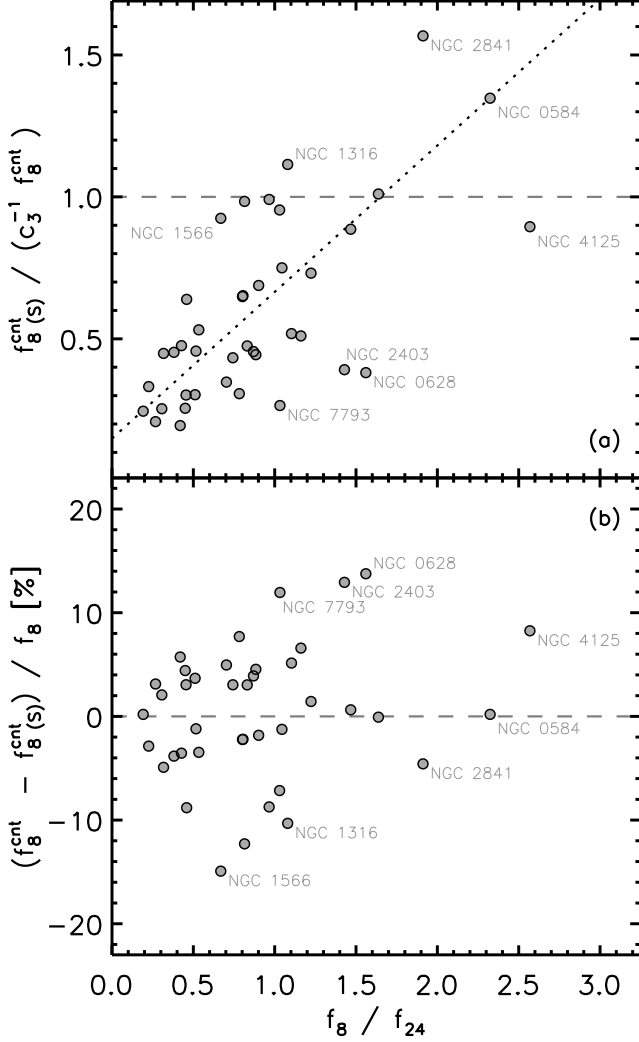


FIG. 4.— (a) The ratio between the spectroscopically determined dust continuum contribution to the IRAC $8\mu\text{m}$ band ($f_{8(\text{S})}^{\text{cnt}}$) and the photometric value given by Equations (5) and (6) with $c_3 = 1$ is correlated to the IRAC $8\mu\text{m}$ over MIPS $24\mu\text{m}$ color in the spectroscopic sample of SINGS galaxies and systematically differs from unity (dashed line). (b) Adopting the linear fit from (a), $c_3 = 0.149 + 0.516f_8/f_{24}$ (dotted line), the difference between the photometrically determined dust continuum flux ($f_{8(\text{S})}^{\text{cnt}}$) and the spectroscopic value (relative to the total IRAC $8\mu\text{m}$ flux) is scattered about zero (dashed line) with an rms of 0.064.

Combining Equations (4) through (7) allows for the determination of c_2 . Minimizing the rms of the error (i.e., the difference between the photometrically and spectroscopically determined values) in the fraction f_8^{afe}/f_8 yields $c_2 = 0.934$. Likewise, adopting $c_1 = 1.53 \times 10^{13}$ in Equation (3) achieves the lowest rms for $(F_8^{\text{afe}} - F_{8(\text{S})}^{\text{afe}})/F_8$, where $F_8 \approx c_1 10^{-23} f_8$. Thus, our photometric prescription for the integrated flux in the five aromatic features we refer to as the $8\mu\text{m}$ complex, calibrated with the spectroscopic sample, becomes

$$F_8^{\text{afe}} = 1.43 \times 10^{-10} \left(f_8^{\text{ns}} - (0.091 + 0.314 f_8/f_{24}) \times (f_{4.5}^{\text{ns}} + f_{5.8}^{\text{ns}})^{0.718} f_{24}^{\text{ns} 0.282} \right), \quad (8)$$

where all of the flux densities are in Janskys and F_8^{afe} has units of $\text{ergs}^{-1} \text{cm}^{-2}$.

4.2.4. Photometric vs. Spectroscopic AFE

Figure 5 demonstrates the agreement between the photometrically determined F_8^{afe} from Equation (8) and the spectroscopically derived $F_{8(\text{S})}^{\text{afe}}$ from Table 2 for the SINGS galaxies comprising the spectroscopic sample. Here the integrated fluxes have been converted to luminosities using the distances provided in Table 1. The lower panel shows that the difference in the methodologies relative to the total luminosity in the $8\mu\text{m}$ band is at worst a 12% effect (including the two apparent outliers in the upper panel which correspond to galaxies with approximately zero aromatic emission) that improves with increasing luminosity in the aromatic features. The rms about zero (for the full luminosity range) is 6%. This systematic error is dominated by uncertainty in the dust continuum at $8\mu\text{m}$.

Individual error bars for the quantity $(L_8^{\text{afe}} - L_{8(\text{S})}^{\text{afe}})/L_8$ were determined both by mathematically propagating the various photometric uncertainties through Equation (8) and by repeating the calculations 1000 times with Monte Carlo resampling of the uncertainties. Both methods were in agreement, and both significantly exceeded the rms quoted above. This is, perhaps, not surprising as scaling the spectra to match the aperture matched photometry eliminated some degree of systematic error from sources such as tilts and/or offsets in the spectra and uncertain extended source corrections in the photometry. Thus, we adopt the $0.06F_8$ systematic error as a representative uncertainty in the measurement of F_8^{afe} . Note, however, that this pertains to the methodology itself and due care should be taken when applying it to data with significantly greater statistical uncertainties.

Similarly, consideration of the galaxies on which these results are based should be taken into account when applying this methodology to other samples. The estimation of the dust continuum at $8\mu\text{m}$ is a model-independent extrapolation of a galaxy's SED and has been shown to be reliable for both dust dominated SEDs with strong aromatic features and stellar dominated SEDs with little to no aromatic emission. Thus, these results are somewhat insensitive to a galaxy's particular properties. However, as an example, in cases of galaxies with very hot dust (e.g., the starburst galaxy SBS 0335–052E; Engelbracht et al. 2008), the color correction given in Equation (7) may be insufficient, resulting in an underestimated dust continuum and a corresponding error in the strength of the aromatic features surpassing that found in this sample.

4.2.5. Alternative Non-Stellar Scaling

The dust decomposition of the stellar-subtracted IRAC $8\mu\text{m}$ flux density given by Equation (5) and discussed in § 4.2.3 is a simple power-law extrapolation of the dust continuum at 4.5 and 24 microns. It is worth noting that an even simpler alternative is a multiplicative scaling of the non-stellar light. For the spectroscopic sample, Figure 6 shows results that are generally comparable to Figure 5b when f_8^{cnt} is instead taken to be $f_8^{\text{ns}} \times 0.19$ (the mean from the PAHFIT values in Table 2). Not surprisingly, the disagreement between the photometric and spectroscopic AFE measurements is marginally poorer in most cases (the overall rms increases from 5.8% to 7.5%) and more significantly so for galaxies with relatively weak or absent aromatic features (e.g., NGC 2841 or NGC 1316). Scaling the non-stellar $8\mu\text{m}$ emission has the advantage of not requiring additional adjacent photometry; however, we caution that systematic errors for galaxies with unusual SEDs (e.g., Houck et al. 2004a; Wu et al. 2007) will be increased as a re-

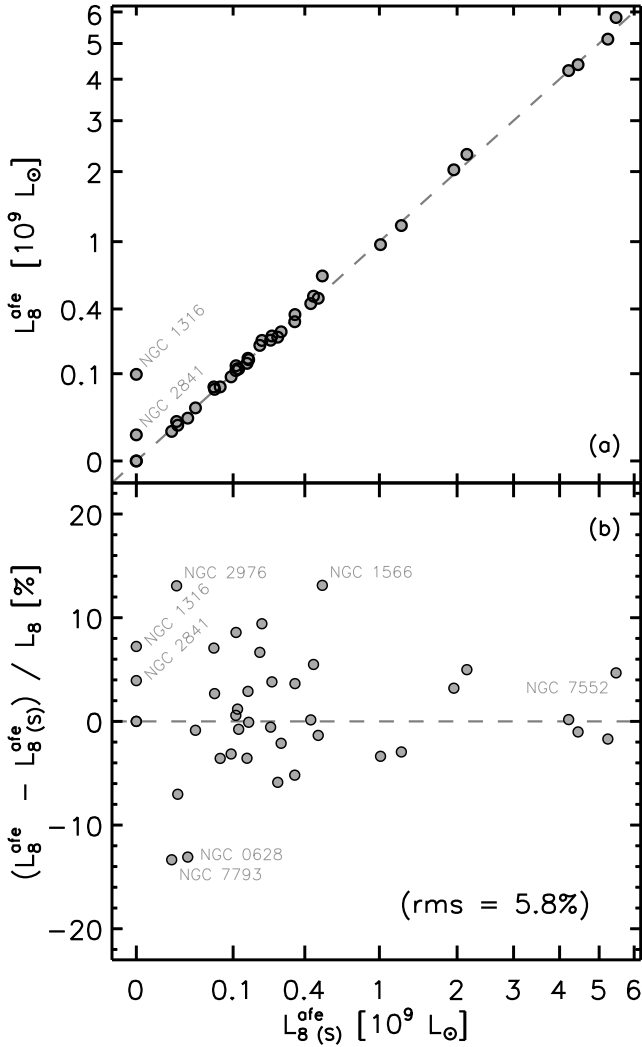


FIG. 5.— (a) For the 40 SINGS galaxies in the spectroscopic sample, the photometrically determined AFE luminosities given by Equation (8) recover the spectroscopic values well (the dashed line indicates equality), with the two apparent outliers corresponding to galaxies with approximately zero aromatic emission. As shown in (b), the maximal difference relative to the total $8\mu\text{m}$ luminosity is 12% with a total rms about zero (dashed line) of 6%.

sult.

4.2.6. Future Improvement

Given the coarse approach of approximating a complex of spectral features with broad-band photometry, the systematic uncertainty quoted in § 4.2.4 is impressive. The most efficient means of improving upon these results is more accurately constraining the dust continuum. For example, Figure 7 demonstrates a 50% reduction in scatter between the photometric and spectroscopic AFE measurements, given a $5.5\mu\text{m}$ band that avoids the aromatic feature at $\lambda = 6.2\mu\text{m}$ and a $10\mu\text{m}$ band that samples the continuum closer to the $8\mu\text{m}$ complex than the MIPS $24\mu\text{m}$ band. These, or complementary, data will be available in the future from the yet to be launched *James Webb Space Telescope* (Gardner et al. 2006).

4.2.7. Mitigated Uncertainties

In § 4.2.4 we quote a modest systematic error in the photometric measurement of aromatic emission in the $8\mu\text{m}$ complex. However, by construction, this uncertainty is

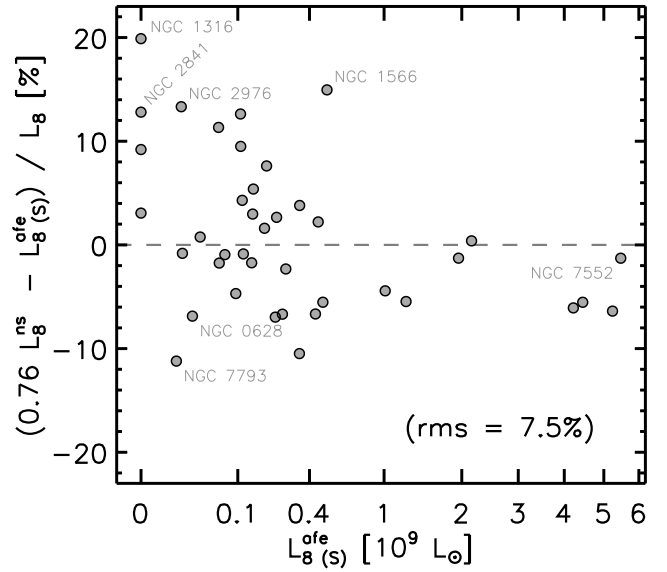


FIG. 6.— Same as Figure 5b, except with photometrically determined AFE luminosities given by $0.76 (= c_2(1-0.19))$ times the non-stellar IRAC $8\mu\text{m}$ luminosity instead of Equation (8). The resulting agreement with the spectroscopic values is generally poorer, although comparable. There is a slight apparent luminosity trend, and, not surprisingly, the simple scaling of the non-stellar light introduces greater errors for those galaxies with very little relative aromatic emission (e.g., NGC 1316).

essentially random and thus mitigated when considering sufficiently large samples of galaxies. For example, summing the spectroscopically and photometrically determined AFE values for the 40 SINGS galaxies in the spectroscopic sample respectively yields $\sum L_{8(s)}^{\text{afe}} = 3.10 \times 10^{10} L_{\odot}$ and $\sum L_8^{\text{afe}} = 3.14 \times 10^{10} L_{\odot}$, which differ by only 1.3%.

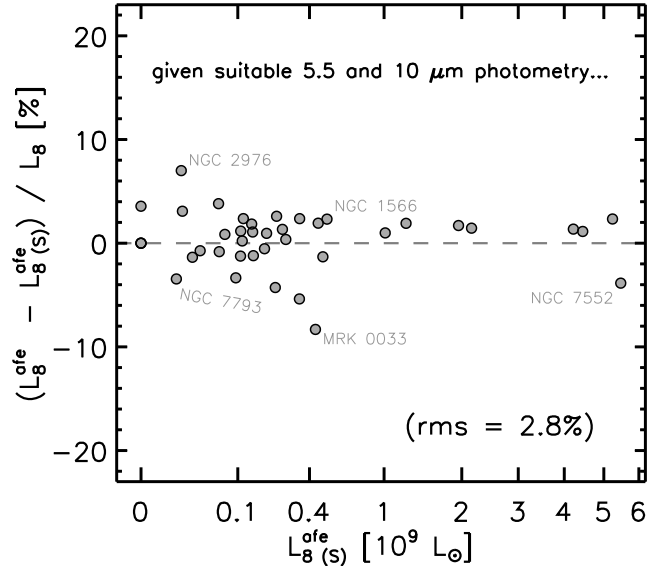


FIG. 7.— Same as Figure 5b, except with dust continuum measurements based on synthetic photometry at $5.5\mu\text{m}$ and $10\mu\text{m}$, demonstrating that future datasets (e.g., from JWST) could further improve the reliability of photometric mid-infrared aromatic feature emission measurements by a factor of two.

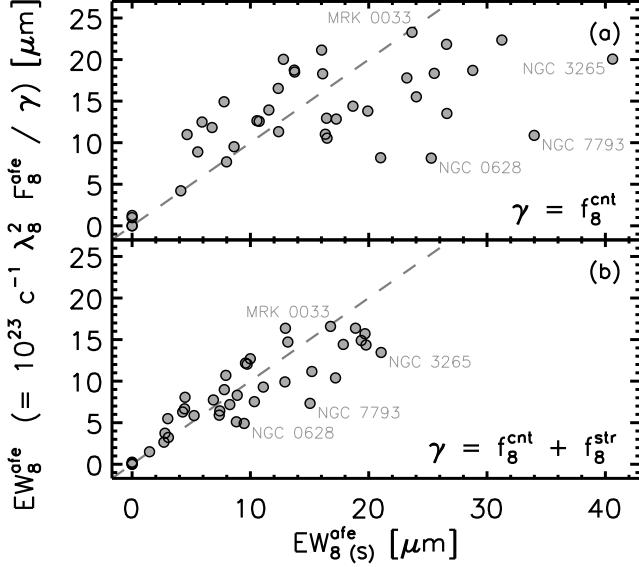


FIG. 8.— Parametrizing the photometrically determined AFE values as equivalent widths is inadvisable, as the agreement between the photometric and spectroscopic values seen in Figure 5 is significantly diminished when dividing by either the relatively uncertain dust continuum (a) or the stellar plus dust continuum (b).

4.2.8. Equivalent Widths

In order to make comparisons between galaxies that are free of distance and luminosity biases, line fluxes are often converted to equivalent widths (EW) by dividing them by the underlying continuum. However, we caution that the agreement between the spectroscopic and photometric methodologies decreases significantly if equivalent widths are used for the latter (compare Figure 5a to Figure 8). This is precisely because the dust continuum is the dominant source of uncertainty in F_8^{afe} and can itself be relatively weak. The scatter between the photometric EW_8^{afe} and the spectroscopic $EW_{8(s)}^{\text{afe}}$ arises in part because an underestimated continuum results in an overestimated aromatic emission strength, doubly inflating the equivalent width, and vice versa. If a distance and luminosity independent measure of the aromatic feature emission is needed for meaningful comparison of different galaxies, a suitable alternative is to normalize F_8^{afe} by the generally larger and better constrained $24\mu\text{m}$ flux or, better yet, the total infrared flux,

$$F_{\text{TIR}} = c \left(\zeta_1 \frac{f_{24}}{\lambda_{24}} + \zeta_2 \frac{f_{70}}{\lambda_{70}} + \zeta_3 \frac{f_{160}}{\lambda_{160}} \right). \quad (9)$$

Here, F_{TIR} corresponds to the 3–1100 μm range, c is the speed of light, λ_X refers to the effective wavelength of band X ($\lambda_{24} = 23.675\mu\text{m}$, $\lambda_{70} = 71.440\mu\text{m}$, $\lambda_{160} = 155.899\mu\text{m}$), and the coefficients $[\zeta_1, \zeta_2, \zeta_3]$ are provided as a function of redshift ($= [1.559, 0.7686, 1.347]$ for $z = 0$) in Figure 7 of Dale & Helou (2002).

5. AFE IN THE LOCAL VOLUME

Using Equations (4)–(7) and the spectral modelling described in § 4.2.1, the IRAC $8\mu\text{m}$ photometry for the LVL galaxies was divided into contributions from aromatic features, the dust continuum, and starlight. Then, Equation (8) was used to determine the integrated flux in the five aromatic features (centered at $\lambda_{\text{rest}} =$

7.42, 7.60, 7.85, 8.33, and $8.61\mu\text{m}$) comprising the $8\mu\text{m}$ complex, and the same systematic uncertainty obtained from the spectroscopic sample ($0.06F_8$) was assumed. The results are provided in Table 3, and Figure 9 depicts the stellar and dust continuum components relative to the observed photometry.

The reliability of this photometric approach was demonstrated for the 40 SINGS galaxies comprising the spectroscopic sample (see § 4.2.4); however, many of the LVL galaxies are significantly less luminous. Whereas the IRAC $8\mu\text{m}$ band luminosity range of the former is $9.9 > \log(L_8/L_\odot) > 7.0$, the LVL galaxies extend from $\log(L_8/L_\odot) = 9.6$ down to $\log(L_8/L_\odot) < 4.3$. The low-luminosity nature of this dwarf galaxy dominated sample is, in fact, what necessitated a photometric prescription for measuring AFE in the first place. However, the decomposition of the emission in the $8\mu\text{m}$ band primarily depends on the relative strengths of the other IRAC and MIPS $24\mu\text{m}$ bands (i.e., the shape or color of the mid-infrared SED). The SINGS spectra (recall Figure 2) span the range from dust dominated SEDs with strong aromatic features to stellar dominated SEDs with little or no aromatic emission. More specifically, the following discussion demonstrates the comparable color ranges of the LVL and spectroscopic samples.

The estimation of the dust continuum at $8\mu\text{m}$ in Equation (8) depends on $(f_{4.5}^{\text{ns}} + f_{5.8}^{\text{ns}})/(f_{24}^{\text{ns}})$, which spans 0.00–0.98 and 0.06–0.73 in the LVL and spectroscopic samples. Likewise, the range of the f_8/f_{24} color, corresponding to the correction term given by Equation (7), for the two samples is 0.03–2.72 and 0.19–2.60, respectively (note that for small f_8/f_{24} this correction becomes negligible). More generally, there is very good agreement between the mid-infrared starlight-to-dust ($f_{3.6}/f_{24}$) distributions of the LVL (0.02–11.81) and spectroscopic (0.03–9.12) galaxies. These color comparisons exclude one outlier in the LVL sample. The corresponding values for UGC 05442 (see Figure 9) are $(f_{4.5}^{\text{ns}} + f_{5.8}^{\text{ns}})/(f_{24}^{\text{ns}}) = 2.43$, $f_8/f_{24} = 12.00$, and $f_{3.6}/f_{24} = 19.58$; however, the spectroscopic sample includes several galaxies similarly dominated by starlight in the mid-infrared (see Figure 2; e.g., NGC 4125).

5.1. An AFE Inventory

As demonstrated in § 4.2.7, the uncertainties in the photometrically determined F_8^{afe} are sufficiently random to allow for an accurate inventory of the aromatic emission in a sample as large as LVL. Summing L_8^{afe} for all 258 galaxies, the total luminosity from the $8\mu\text{m}$ complex of aromatic features is $9.49 \times 10^{43} \text{ erg/s}$ or $2.47 \times 10^{10} L_\odot$. This includes upper limits for 38 galaxies and the assumption that all of the $8\mu\text{m}$ light is aromatic for the 15 galaxies without constraints on F_8^{afe} (see Table 1). However, excluding these 53 galaxies decreases the total luminosity by only 0.05%, which is less than the 1.9% propagated systematic uncertainty.

Figure 10 depicts this inventory in the form of a cumulative histogram, where the 10 galaxies with the highest L_8^{afe} are labeled. It is worth noting that these 10 galaxies are responsible for 70% of the total aromatic luminosity in LVL. Likewise, 24 galaxies account for 90%. From linear fits to L_8^{afe} versus the absolute B magnitude provided in Dale et al. (2009) and the total infrared luminosity given by Equation (9), the $10^{\text{th}}/24^{\text{th}}$ galaxy corresponds to $M_B = -18.82/-18.22 \pm 0.87$ and $L_{\text{TIR}} = 10^{9.54/9.25 \pm 0.17} L_\odot$. Here, the uncertainties are taken to be the rms of the scatter about the fits.

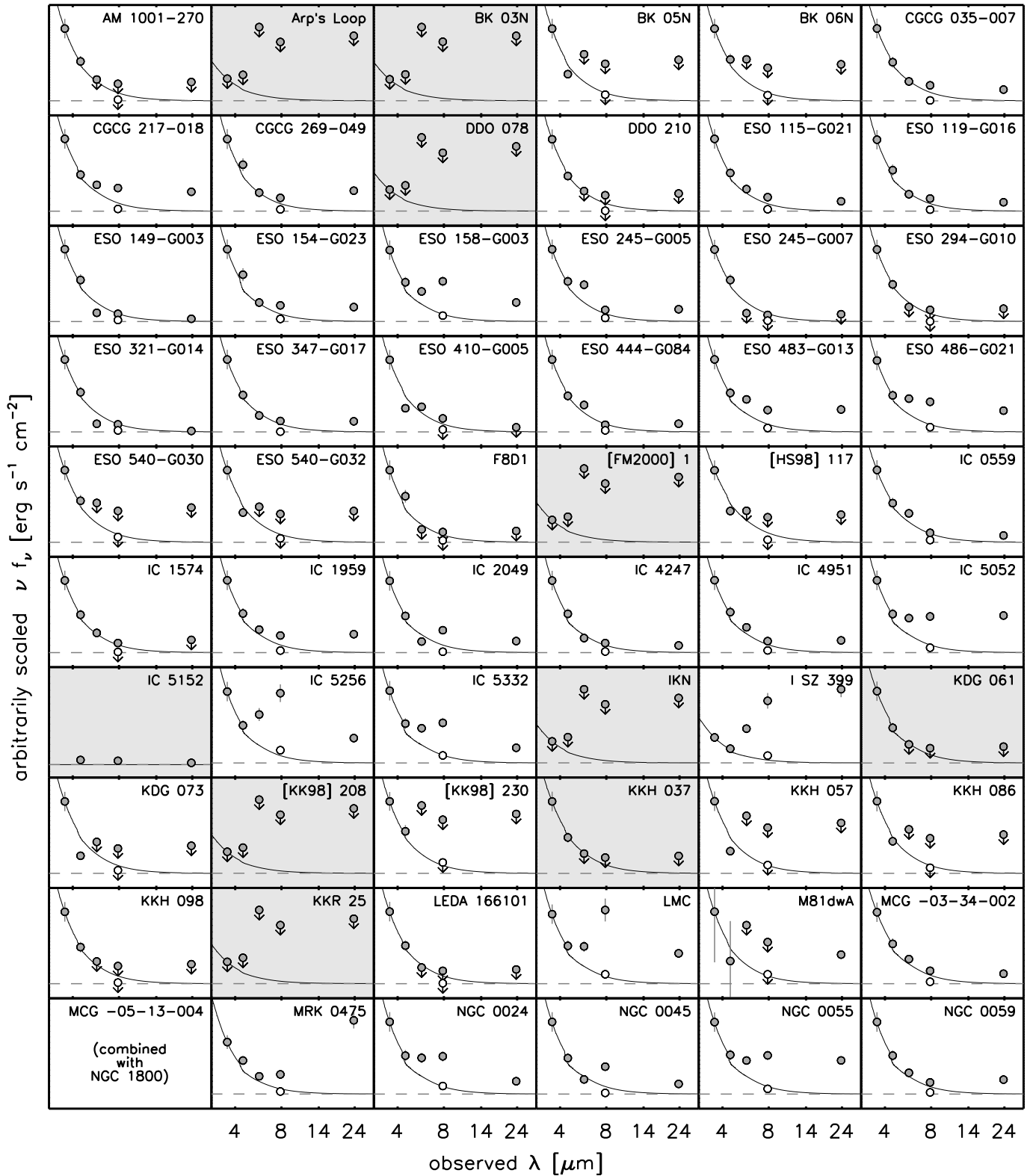


FIG. 9.— Thumbnail SEDs for each LVL galaxy showing the IRAC and MIPS $24\mu\text{m}$ photometry (filled circles) with error bars, the tailored stellar model (solid line), and the calculated dust continuum contribution to the IRAC $8\mu\text{m}$ band (open circle). Zero is indicated by the dashed line, arrows pointing down from data points signify upper limits, and shaded plots correspond to those cases where the dust continuum contribution could not be determined.

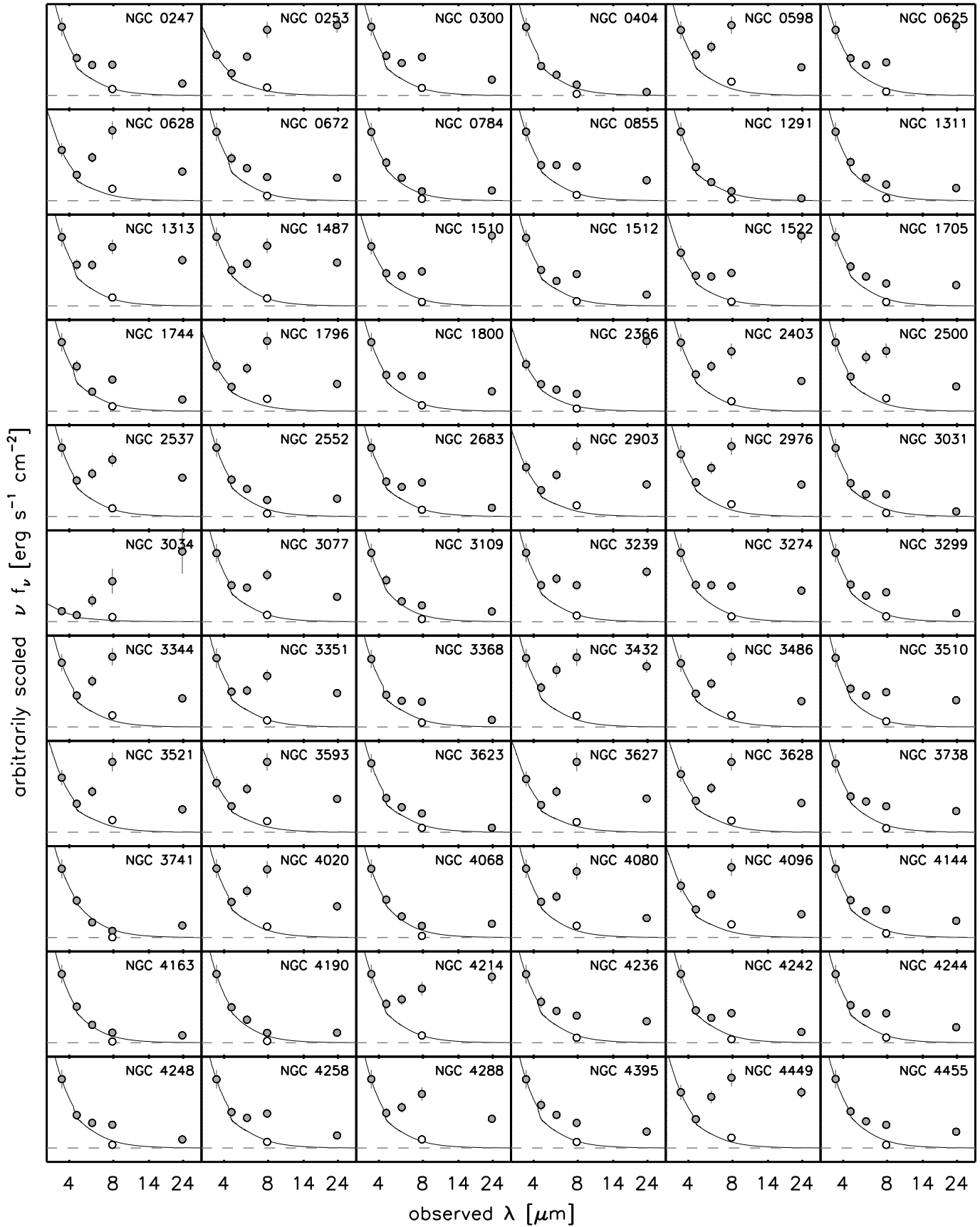


FIG. 9.—Continued

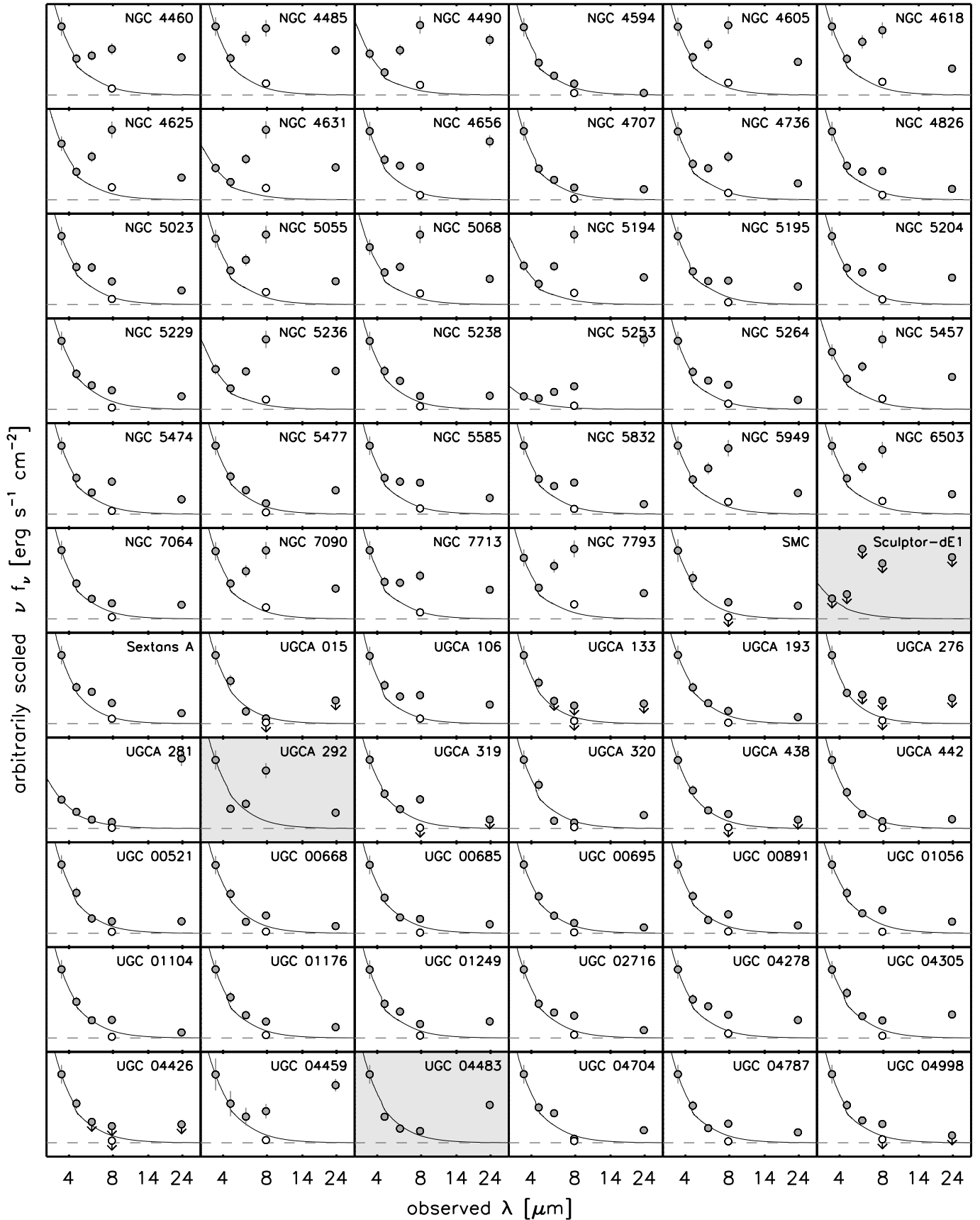


FIG. 9.—Continued

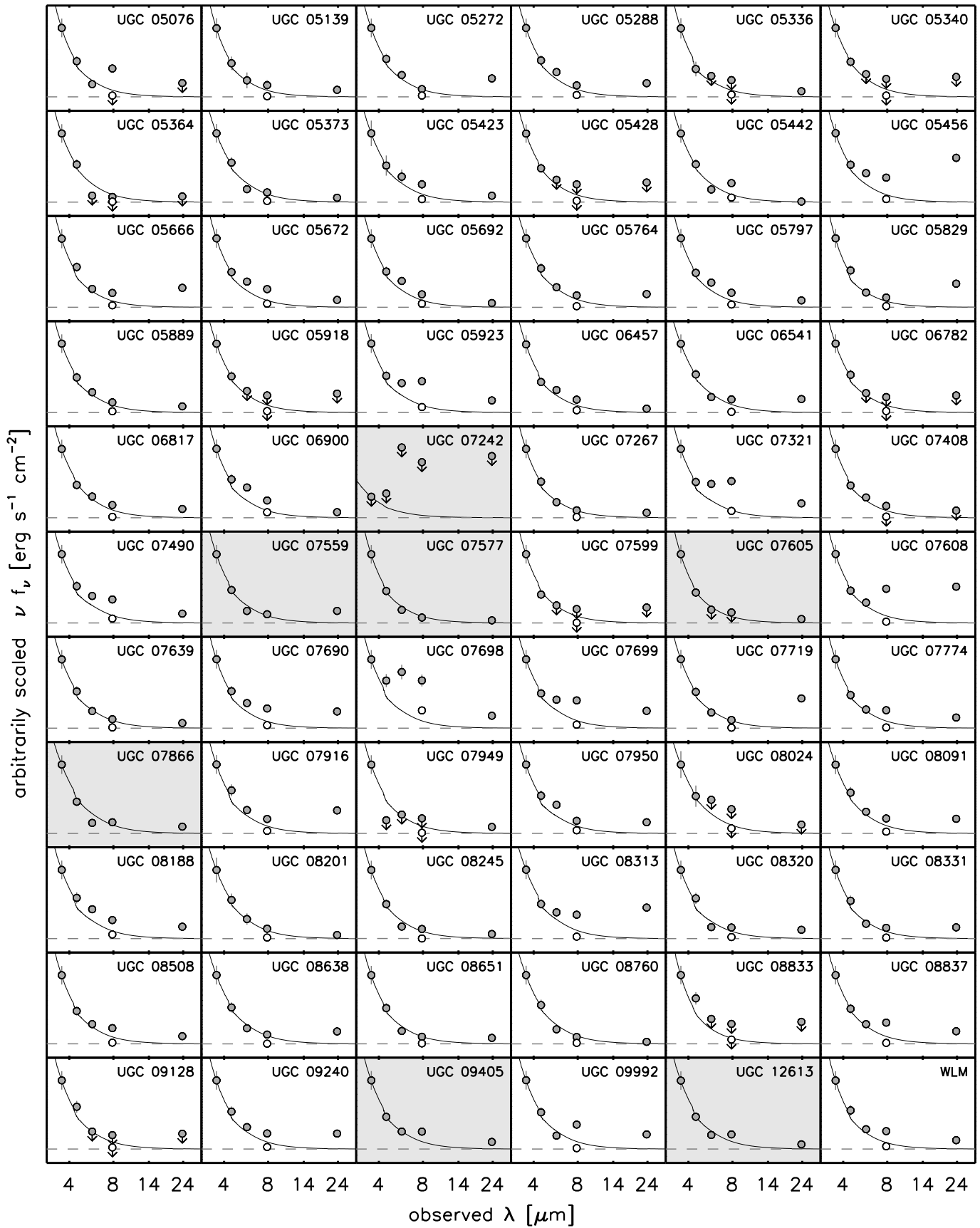


FIG. 9.—Continued

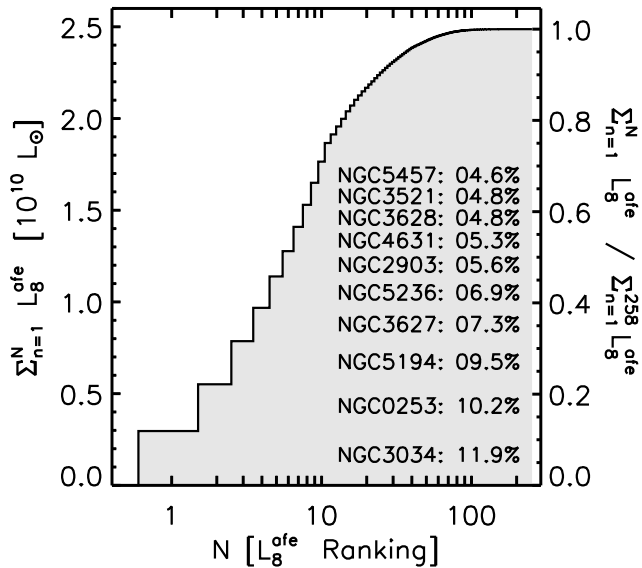


FIG. 10.— Cumulative histogram of the photometrically determined AFE luminosities for the 258 LVL galaxies (on absolute and relative scales on the left and right axes, respectively). This is based on upper limits for 43 galaxies and the assumption that $F_8^{\text{afe}} \equiv F_8$ for 10 galaxies without AFE measurements; however, the contributions of these 53 galaxies represent only 0.05% of the total. The galaxies are ordered from left to right according to decreasing AFE luminosity, and the 10 highest contributors are labeled.

The LVL survey represents 52% of the local volume within 11 Mpc (see § 2), or approximately 2800 cubic Mpc. Thus, the mean density of aromatic emission from the $8\mu\text{m}$ complex is $8.8 \times 10^6 L_{\odot} \text{Mpc}^{-3}$. Adopting the mean ratio $< F_{\text{mir}(S)}^{\text{afe}} / F_{8(S)}^{\text{afe}} > = 1.89$ from the spectroscopic sample (see Table 2), the numbers above translate into a total LVL aromatic emission luminosity and mean density of $4.67 \times 10^{10} L_{\odot}$ and $1.7 \times 10^7 L_{\odot} \text{Mpc}^{-3}$, respectively, for the mid-infrared wavelength range $5.5\mu\text{m} < \lambda < 20\mu\text{m}$. This scaling is based on the approximately inner kiloparsec of the 40 SINGS galaxies in the spectroscopic sample; however, the global photometry used for the LVL galaxies is similarly dominated by the central region.

5.2. Relative AFE

The primary purpose of this paper is to demonstrate the efficacy of our photometric prescription for measuring the strength of the $8\mu\text{m}$ aromatic features and to present such measurements for the LVL sample of galaxies. However, we conclude this section by characterizing these LVL AFE measurements relative to other galaxy properties addressed in this study.

5.2.1. AFE Ratios

For the reasons outlined in § 4.2.8, casting the LVL aromatic feature emission measurements as equivalent widths (i.e., dividing them by the corresponding continua at $8\mu\text{m}$) is not particularly illuminating. Therefore, we consider instead their ratio to other less uncertain probes of dust emission: the total infrared (see Equation (9) and Dale & Helou (2002)), the total IRAC $8\mu\text{m}$ emission, and the total dust emission at $8\mu\text{m}$.

In comparison to the integrated luminosity in the aromatic features, the total 3–1100 μm infrared luminosity of the LVL galaxies is $L_{\text{TIR}} = 4.86 \times 10^{11} L_{\odot}$. This includes 59 upper limits which only amount to 0.12%. Thus, the fraction of the total

infrared luminosity in the local volume contributed by aromatic features in the $8\mu\text{m}$ complex and $5.5\mu\text{m} < \lambda < 20\mu\text{m}$ range is 5.1 and 9.6 percent, respectively (recall the factor of 1.89 from § 5.1). For an individual galaxy, the $8\mu\text{m}$ complex features contribute, on average, 2.5% to the total infrared (see Figure 11a), approximately half that of the SINGS galaxies (Smith et al. 2007b).

In contrast to $F_8^{\text{afe}}/F_{\text{TIR}}$, the ratio of f_8^{afe} over the total IRAC $8\mu\text{m}$ flux density shown in Figure 11b skews towards larger values. This dominance of the aromatic features has resulted in the occasional use of the observed $8\mu\text{m}$ emission as a proxy for AFE. Such a generalization is clearly problematic given the substantial range in f_8^{afe}/f_8 from galaxy to galaxy. For the LVL sample, this ratio spans 0–80% with an abrupt decline in values larger than 70%. The distribution becomes narrower when only non-stellar emission is considered (see Figure 11c); however, $f_8^{\text{afe}}/f_8^{\text{ns}} \simeq f_8^{\text{afe}}/(f_8^{\text{afe}} + f_8^{\text{cnt}})$ still potentially ranges from 0% to greater than 90%. Note that the peak in the lowest bins of both Figures 11b and 11c is likely the result of the approximately 6% uncertainty coupled with our criterion that the measured aromatic emission be greater than or equal to zero.

5.2.2. AFE Ratio vs. TIR

The fact that the LVL galaxies have both a lower average luminosity and a lesser mean $F_8^{\text{afe}}/F_{\text{TIR}}$ than the SINGS galaxies comprising the spectroscopic sample (Figure 11a) suggests a relationship between these properties. Figure 12 confirms that the aromatic feature emission to total infrared ratio is correlated with the total infrared luminosity (the Spearman rank-order coefficient is $r_s = 0.66$), albeit with significant scatter (despite the inverse dependence, the positive correlation with L_{TIR} is stronger than with the $24\mu\text{m}$, $8\mu\text{m}$, or B band luminosities). This dependence may (see § 5.2.3) simply be a repackaging of the luminosity-metallicity relationship shown in Figure 3 and previously reported trends between metallicity and the relative strength of the $8\mu\text{m}$ aromatic features (see, e.g., Engelbracht et al. 2008). However, this result is unique with regard to the large sample size considered. Note that the correlation weakens ($r_s = 0.54$) if the total dust at $8\mu\text{m}$ is considered rather than just the aromatic portion.

5.2.3. AFE Ratio vs. Oxygen Abundance

For a sample of starburst galaxies, Engelbracht et al. (2008) found a weak correlation between oxygen abundance and the equivalent width of emission from the same $8\mu\text{m}$ complex of aromatic features considered here. A stronger correlation resulted when comparing EW_8^{afe} to the hardness of the radiation field (see, also, Jackson et al. 2006). The opposite was reported by Wu et al. (2009) for the case of dwarf galaxies; however, their probe of aromatic emission was limited to the $f_8/f_{3.6}$ color. Looking at HII regions in M101, Gordon et al. (2008) found the same correlation with radiation field hardness as Engelbracht et al. (2008), but no corresponding trend with metallicity.

For the LVL galaxies, we find a similar correlation as Engelbracht et al. (2008) between oxygen abundance and the relative strength of the AFE (Figure 13). There is significant scatter; however, a Spearman rank-order test yields $r_s = 0.71$. Given the comparable trend with L_{TIR} found in Figure 12 and the well-known L-Z correlation shown in Figure 3, this raises the question of whether metallicity or luminosity is more fundamentally related to aromatic feature emission. The Spear-

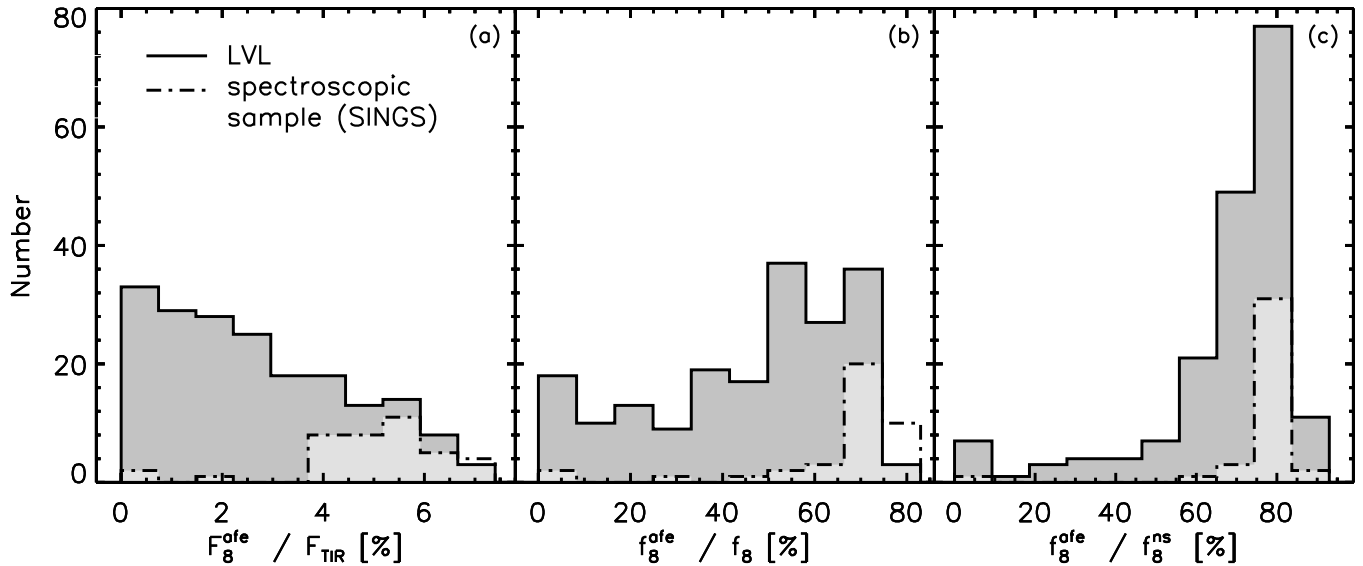


FIG. 11.— Histograms of the photometrically determined $8\mu\text{m}$ AFE relative to the (a) total infrared ($3-1100\mu\text{m}$) emission, (b) total IRAC $8\mu\text{m}$ emission, and (c) total IRAC $8\mu\text{m}$ dust emission for the 40 SINGS galaxies in the spectroscopic sample and the approximately 200 LVL galaxies with reliable values (i.e., no upper limits for either quantity).

man correlation coefficient is smaller for the total infrared luminosity than the oxygen abundance, despite the approximately $0.1-0.2$ dex systematic errors expected for the latter (see § 3.2), implying that metallicity is the dominant factor. This is further supported by partial correlation coefficients computed for the subset of galaxies with total infrared luminosity, aromatic emission, and oxygen abundance measurements.

The correlation with oxygen abundance is weaker when the ratio of AFE to the total IRAC $8\mu\text{m}$ flux is considered instead of $F_8^{\text{afe}}/F_{\text{TIR}}$ and is essentially gone when the stellar component of the IRAC $8\mu\text{m}$ flux is removed (Figure 14). This may imply that while metallicity plays a role in the ratio of aromatic molecules to total dust content (i.e., the TIR), the excitation of those molecules, and thus, the relative amounts of

AFE and dust emission at $8\mu\text{m}$, are governed by other properties such as star formation and/or the hardness and intensity of the local radiation field.

6. SUMMARY AND CONCLUSIONS

We have presented a purely photometric methodology for measuring the strength of the emission from mid-infrared aromatic features in nearby galaxies that are either too faint, too numerous, or too spatially extended for spectroscopy to be feasible. *Spitzer* IRAC (3.6 , 4.5 , and $5.8\mu\text{m}$) and MIPS $24\mu\text{m}$ photometry are used to disentangle contributions to the IRAC $8\mu\text{m}$ flux density from starlight, the dust continuum,

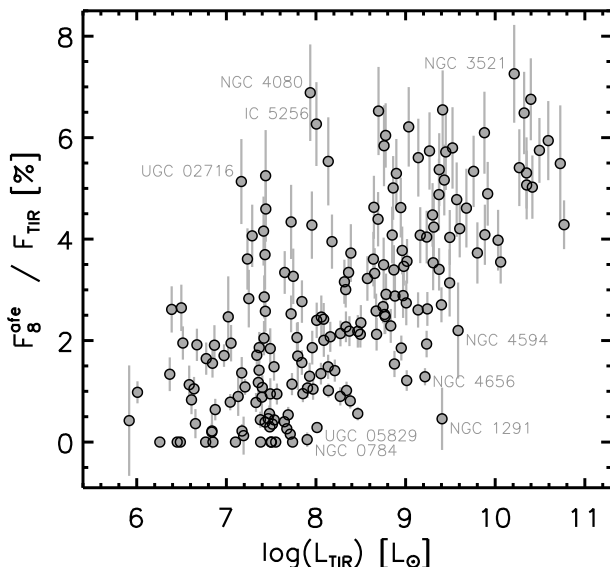


FIG. 12.— The photometrically determined $8\mu\text{m}$ AFE to total infrared ($3-1100\mu\text{m}$) emission ratio versus the total infrared luminosity for the 189 LVL galaxies unaffected by upper limits. The corresponding Spearman rank-order correlation coefficient is 0.66 .

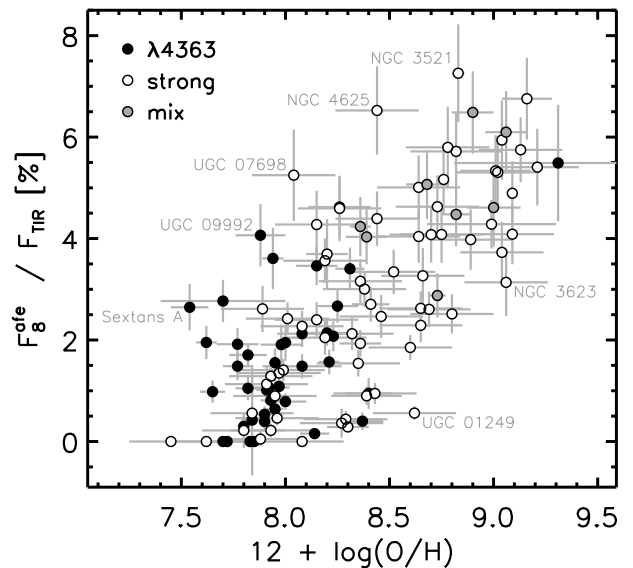


FIG. 13.— The photometrically determined $8\mu\text{m}$ AFE to total infrared ($3-1100\mu\text{m}$) emission ratio versus oxygen abundance for the 114 LVL galaxies unaffected by upper limits or missing data. Compiled from the literature, the oxygen abundances (the shading of the circle reflects the measurement method) have an expected systematic error of $0.1-0.2$ in addition to the error bars shown here. The corresponding Spearman rank-order correlation coefficient is 0.71 .

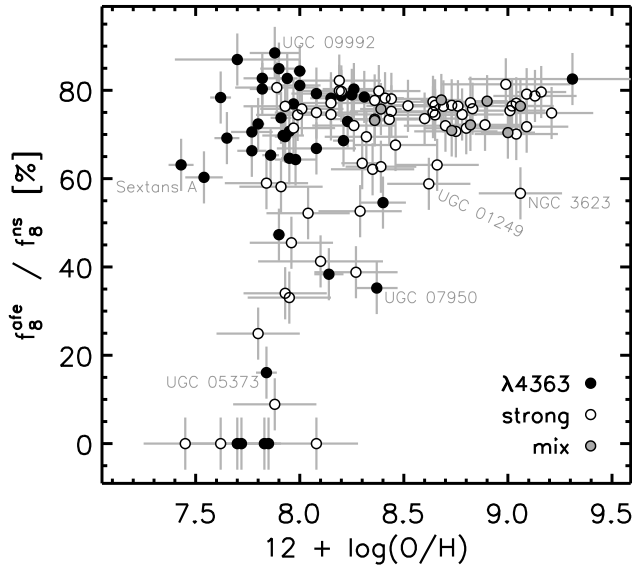


FIG. 14.— The ratio of aromatic to total dust emission at $8\mu\text{m}$ versus oxygen abundance (the shading of the circle reflects the measurement method). Lack of a correlation (compared to Figure 13) may imply that metallicity affects the abundance of aromatic molecules relative to the total dust content, while other factors (such as star formation and/or the hardness of the radiation field) affect the excitation of the aromatic molecules.

and the $8\mu\text{m}$ complex of aromatic features. The latter is then calibrated to approximate the integrated flux one would obtain spectroscopically for the individual features at 7.42, 7.60, 7.85, 8.33, and $8.61\mu\text{m}$. With carefully matched photometry, we demonstrate that the photometric technique recovers the spectroscopically derived aromatic fraction of the total $8\mu\text{m}$ luminosity in a sample of 40 SINGS galaxies with a maximal relative difference of 12% and an rms of 6%. Given suitable 5.5 and $10\mu\text{m}$ photometry, the rms could decrease by a factor of two in future studies.

The photometric approach was then used to measure aromatic emission from galaxies in the Local Volume Legacy sample, a *Spitzer* IRAC and MIPS survey of a statistically complete and nearly volume-limited sample of 258 nearby galaxies within 11 Mpc. In doing so, we have presented the first inventory of aromatic feature emission for a statistically complete sample of star-forming galaxies in the local universe. The total luminosity in the LVL sample resulting from the $8\mu\text{m}$ complex of five strong aromatic features is $2.47 \times 10^{10} L_{\odot}$ with a mean volume density of $8.8 \times$

$10^6 L_{\odot} \text{Mpc}^{-3}$. The corresponding values for all mid-infrared aromatic features in the wavelength range $5.5\mu\text{m} < \lambda < 20\mu\text{m}$ are larger by a factor of approximately 1.9. Twenty-four of the LVL galaxies, corresponding to $M_B > -18.22 \pm 0.87$ and $L_{\text{TIR}} > 10^{9.25 \pm 0.17} L_{\odot}$, are responsible for 90% of the total $8\mu\text{m}$ aromatic luminosity.

For a given LVL galaxy, the $8\mu\text{m}$ complex features contribute, on average, 2.5% of the total infrared luminosity, or roughly half that of the more luminous SINGS galaxies. As a whole, the combined contribution for the LVL sample is 5.1%. With respect to the total dust emission in the IRAC $8\mu\text{m}$ band, the aromatic contribution ranges from 0% to 90%. Similarly, the aromatic features are responsible for between 0% and 80% of all the light in the IRAC $8\mu\text{m}$ band.

Oxygen abundances compiled from the literature were presented for 129 of the 258 LVL galaxies. These are shown to follow the well-known luminosity-metallicity relationship with a best fit for the IRAC $4.5\mu\text{m}$ band of $12 + \log(\text{O}/\text{H}) = 5.06 \pm 0.04 - (0.164 \pm 0.002)M_{4.5}$. We find that the total infrared luminosity and oxygen abundance correlate weakly with the aromatic to total infrared flux ratio and tentatively identify the latter relationship as being more fundamental. The trend with oxygen abundance breaks down when the total dust emission at $8\mu\text{m}$ is used to scale the aromatic emission instead of the total infrared emission from 3– $1100\mu\text{m}$. One possible explanation for this is that metallicity affects the abundance of aromatic molecules, while other factors such as star formation and/or the local radiation field determine their excitation.

This work is part of the *Spitzer Space Telescope* Legacy Science Program and was supported by National Aeronautics and Space Administration (NASA) through contract 1336000 issued by the Jet Propulsion Laboratory (JPL), California Institute of Technology (Caltech) under NASA contract 1407. Additionally, this publication makes use of data products from the Two-Micron All Sky Survey, which is a joint project of the University of Massachusetts and the Infrared Processing and Analysis Center (IPAC) at Caltech, funded by NASA and the National Science Foundation. This research has made use of the NASA/IPAC Extragalactic Database, which is operated by JPL/Caltech, under contract with NASA. Finally, we thank the referee for helpful comments and suggestions that resulted in an improved paper.

REFERENCES

- Adelman-McCarthy, J. K., et al. 2008, *ApJS*, 175, 297
Aguero, E. L., & Carranza, G. J. 1985, *Ap&SS*, 117, 271
Aguero, E. L., & Paolantonio, S. 1997, *AJ*, 114, 102
Alloin, D., Collin-Souffrin, S., Joly, M., & Vigroux, L. 1979, *A&A*, 78, 200
Bresolin, F. 2007, *ApJ*, 656, 186
Bresolin, F., Garnett, D. R., & Kennicutt, Jr., R. C. 2004, *ApJ*, 615, 228
Bresolin, F., & Kennicutt, Jr., R. C. 2002, *ApJ*, 572, 838
Bresolin, F., Kennicutt, Jr., R. C., & Garnett, D. R. 1999, *ApJ*, 510, 104
Bresolin, F., Schaerer, D., González Delgado, R. M., & Stasińska, G. 2005, *A&A*, 441, 981
Buckalew, B. A., Kobulnicky, H. A., & Dufour, R. J. 2005, *ApJS*, 157, 30
Castellanos, M., Díaz, A. I., & Terlevich, E. 2002, *MNRAS*, 329, 315
Cedr s, B., & Cepa, J. 2002, *A&A*, 391, 809
Christensen, T., Petersen, L., & Gammelgaard, P. 1997, *A&A*, 322, 41
Chun, M.-S. 1983, *Journal of Korean Astronomical Society*, 16, 1
Cohen, M., Wheaton, W. A., & Megeath, S. T. 2003, *AJ*, 126, 1090
Crockett, N. R., Garnett, D. R., Massey, P., & Jacoby, G. 2006, *ApJ*, 637, 741
Croxall, K. V., van Zee, L., Lee, H., Skillman, E. D., Lee, J. C., C t , S., Kennicutt, R. C., & Miller, B. W. 2009, *ApJ*, 705, 723
Dalcanton, J. J., et al. 2009, *ApJS*, 183, 67
Dale, D. A., & Helou, G. 2002, *ApJ*, 576, 159
Dale, D. A., et al. 2007, *ApJ*, 655, 863
—, 2009, *ApJ*, 703, 517
Davidson, K., & Kinman, T. D. 1982, *PASP*, 94, 634
De Robertis, M. M. 1987, *ApJ*, 316, 597
D az, A. I., Castellanos, M., Terlevich, E., & Luisa Garc a-Vargas, M. 2000, *MNRAS*, 318, 462
D az, A. I., Terlevich, E., Vilchez, J. M., Pagel, B. E. J., & Edmunds, M. G. 1991, *MNRAS*, 253, 245
Disney, M. J., & Pottasch, S. R. 1977, *A&A*, 60, 43
Draine, B. T., & Li, A. 2007, *ApJ*, 657, 810

- Dufour, R. J., Talbot, Jr., R. J., Jensen, E. B., & Shields, G. A. 1980, *ApJ*, 236, 119
- Dutil, Y., & Roy, J.-R. 1999, *ApJ*, 516, 62
- Edmunds, M. G., & Pagel, B. E. J. 1984, *MNRAS*, 211, 507
- Engelbracht, C. W., Gordon, K. D., Rieke, G. H., Werner, M. W., Dale, D. A., & Latter, W. B. 2005, *ApJ*, 628, L29
- Engelbracht, C. W., Rieke, G. H., Gordon, K. D., Smith, J.-D. T., Werner, M. W., Moustakas, J., Willmer, C. N. A., & Vanzi, L. 2008, *ApJ*, 678, 804
- Fazio, G. G., et al. 2004, *ApJS*, 154, 10
- Ferguson, A. M. N., Gallagher, J. S., & Wyse, R. F. G. 1998, *AJ*, 116, 673
- French, H. B. 1980, *ApJ*, 240, 41
- Froeblich, D., & Meusinger, H. 2000, *A&AS*, 145, 229
- Gallagher, J. S., Garnavich, P. M., Berlind, P., Challis, P., Jha, S., & Kirshner, R. P. 2005, *ApJ*, 634, 210
- Gallagher, III, J. S., & Hunter, D. A. 1989, *AJ*, 98, 806
- Gardner, J. P., et al. 2006, *Space Science Reviews*, 123, 485
- Garnett, D. R., & Kennicutt, Jr., R. C. 1994, *ApJ*, 426, 123
- Garnett, D. R., Kennicutt, Jr., R. C., & Bresolin, F. 2004, *ApJ*, 607, L21
- Garnett, D. R., & Shields, G. A. 1987, *ApJ*, 317, 82
- Garnett, D. R., Shields, G. A., Skillman, E. D., Sagan, S. P., & Dufour, R. J. 1997, *ApJ*, 489, 63
- Gil de Paz, A., Zamorano, J., & Gallego, J. 2000a, *A&A*, 361, 465
- Gil de Paz, A., Zamorano, J., Gallego, J., & Domínguez, F. d. B. 2000b, *A&AS*, 145, 377
- Gil de Paz, A., et al. 2007, *ApJ*, 661, 115
- Gonzalez-Delgado, R. M., et al. 1994, *ApJ*, 437, 239
- Gonzalez-Riestra, R., Rego, M., & Zamorano, J. 1988, *A&A*, 202, 27
- Gordon, K. D., Engelbracht, C. W., Rieke, G. H., Misselt, K. A., Smith, J.-D. T., & Kennicutt, Jr., R. C. 2008, *ApJ*, 682, 336
- Guseva, N. G., Izotov, Y. I., & Thuan, T. X. 2000, *ApJ*, 531, 776
- Hawley, S. A. 1978, *ApJ*, 224, 417
- Hidalgo-Gómez, A. M., Masegosa, J., & Olofsson, K. 2001, *A&A*, 369, 797
- Hidalgo-Gómez, A. M., & Olofsson, K. 2002, *A&A*, 389, 836
- Hodge, P., & Miller, B. W. 1995, *ApJ*, 451, 176
- Hopp, U., & Schulte-Ladbeck, R. E. 1991, *A&A*, 248, 1
- Houck, J. R., et al. 2004a, *ApJS*, 154, 211
- 2004b, *ApJS*, 154, 18
- Hunter, D. A., Gallagher, J. S., & Rautenkranz, D. 1982, *ApJS*, 49, 53
- Hunter, D. A., & Gallagher, III, J. S. 1985, *ApJS*, 58, 533
- Hunter, D. A., & Hoffman, L. 1999, *AJ*, 117, 2789
- Izotov, Y. I., Stasińska, G., Meynet, G., Guseva, N. G., & Thuan, T. X. 2006, *A&A*, 448, 955
- Izotov, Y. I., Thuan, T. X., & Lipovetsky, V. A. 1994, *ApJ*, 435, 647
- 1997, *ApJS*, 108, 1
- Izotov, Y. I., Thuan, T. X., & Stasińska, G. 2007, *ApJ*, 662, 15
- Jackson, D. C., et al. 2006, *ApJ*, 646, 192
- Johnson, R. A., Lawrence, A., Terlevich, R., & Carter, D. 1997, *MNRAS*, 287, 333
- Kennicutt, R., Balick, B., & Heckman, T. 1980, *PASP*, 92, 134
- Kennicutt, Jr., R. C., Bresolin, F., & Garnett, D. R. 2003a, *ApJ*, 591, 801
- Kennicutt, Jr., R. C., & Garnett, D. R. 1996, *ApJ*, 456, 504
- Kennicutt, Jr., R. C., Lee, J. C., Funes, José G., S. J., Sakai, S., & Akiyama, S. 2008, *ApJS*, 178, 247
- Kennicutt, Jr., R. C., & Skillman, E. D. 2001, *AJ*, 121, 1461
- Kennicutt, Jr., R. C., et al. 2003b, *PASP*, 115, 928
- Kewley, L. J., & Ellison, S. L. 2008, *ApJ*, 681, 1183
- Kewley, L. J., Jansen, R. A., & Geller, M. J. 2005, *PASP*, 117, 227
- Kinman, T. D., & Hintzen, P. 1981, *PASP*, 93, 405
- Kniazev, A. Y., Grebel, E. K., Hao, L., Strauss, M. A., Brinkmann, J., & Fukugita, M. 2003, *ApJ*, 593, L73
- Kniazev, A. Y., Grebel, E. K., Pustilnik, S. A., Pramskij, A. G., & Zucker, D. B. 2005, *AJ*, 130, 1558
- Kniazev, A. Y., Pustilnik, S. A., Grebel, E. K., Lee, H., & Pramskij, A. G. 2004, *ApJS*, 153, 429
- Kobulnicky, H. A., Kennicutt, Jr., R. C., & Pizagno, J. L. 1999, *ApJ*, 514, 544
- Kobulnicky, H. A., & Skillman, E. D. 1996, *ApJ*, 471, 211
- 1997, *ApJ*, 489, 636
- Kobulnicky, H. A., Skillman, E. D., Roy, J.-R., Walsh, J. R., & Rosa, M. R. 1997, *ApJ*, 477, 679
- Lagache, G., Puget, J.-L., & Dole, H. 2005, *ARA&A*, 43, 727
- Lee, H., Grebel, E. K., & Hodge, P. W. 2003a, *A&A*, 401, 141
- Lee, H., McCall, M. L., Kingsburgh, R. L., Ross, R., & Stevenson, C. C. 2003b, *AJ*, 125, 146
- Lee, H., & Skillman, E. D. 2004, *ApJ*, 614, 698
- Lee, H., Skillman, E. D., Cannon, J. M., Jackson, D. C., Gehrz, R. D., Polomski, E. F., & Woodward, C. E. 2006, *ApJ*, 647, 970
- Lee, H., Skillman, E. D., & Venn, K. A. 2005, *ApJ*, 620, 223
- Lee, H., Zucker, D. B., & Grebel, E. K. 2007, *MNRAS*, 376, 820
- Lee, J. C., et al. 2009, *ApJ*, 706, 599
- 2010, in preparation
- Leger, A., & Puget, J. L. 1984, *A&A*, 137, L5
- Leitherer, C., et al. 1999, *ApJS*, 123, 3
- Li, A., & Draine, B. T. 2001, *ApJ*, 554, 778
- Liang, Y. C., Hu, J. Y., Liu, F. S., & Liu, Z. T. 2007, *AJ*, 134, 759
- López-Sánchez, Á. R., Esteban, C., García-Rojas, J., Peimbert, M., & Rodríguez, M. 2007, *ApJ*, 656, 168
- Loveday, J. 1996, *MNRAS*, 278, 1025
- Lu, N., et al. 2003, *ApJ*, 588, 199
- Madden, S. C. 2000, *New Astronomy Review*, 44, 249
- Madden, S. C., Galliano, F., Jones, A. P., & Sauvage, M. 2006, *A&A*, 446, 877
- Magrini, L., Leisy, P., Corradi, R. L. M., Perinotto, M., Mampaso, A., & Vílchez, J. M. 2005, *A&A*, 443, 115
- Magrini, L., Vílchez, J. M., Mampaso, A., Corradi, R. L. M., & Leisy, P. 2007, *A&A*, 470, 865
- Martin, C. L. 1997, *ApJ*, 491, 561
- Martin, P., & Belley, J. 1997, *A&A*, 321, 363
- Masegosa, J., Moles, M., & Campos-Aguilar, A. 1994, *ApJ*, 420, 576
- Masegosa, J., Moles, M., & del Olmo, A. 1991, *A&A*, 249, 505
- Matteucci, F., & Tosi, M. 1985, *MNRAS*, 217, 391
- McCall, M. L., Rybski, P. M., & Shields, G. A. 1981, *PASP*, 93, 273
- 1985, *ApJS*, 57, 1
- McGaugh, S. S. 1991, *ApJ*, 380, 140
- Meurer, G. R., Freeman, K. C., Dopita, M. A., & Cacciari, C. 1992, *AJ*, 103, 60
- Miller, B. W. 1996, *AJ*, 112, 991
- Miller, B. W., & Hodge, P. 1996, *ApJ*, 458, 467
- Moles, M., Aparicio, A., & Masegosa, J. 1990, *A&A*, 228, 310
- Moustakas, J., & Kennicutt, Jr., R. C. 2006a, *ApJS*, 164, 81
- 2006b, *ApJ*, 651, 155
- Oey, M. S., & Kennicutt, Jr., R. C. 1993, *ApJ*, 411, 137
- Pagel, B. E. J., Edmunds, M. G., Blackwell, D. E., Chun, M. S., & Smith, G. 1979, *MNRAS*, 189, 95
- Pagel, B. E. J., Edmunds, M. G., & Smith, G. 1980, *MNRAS*, 193, 219
- Pahre, M. A., Ashby, M. L. N., Fazio, G. G., & Willner, S. P. 2004, *ApJS*, 154, 235
- Peña, M., Stasińska, G., & Richer, M. G. 2007, *A&A*, 476, 745
- Pérez-Montero, E., & Díaz, A. I. 2003, *MNRAS*, 346, 105
- Pustilnik, S., Zasov, A., Kniazev, A., Pramskij, A., Ugryumov, A., & Burenkov, A. 2003, *A&A*, 400, 841
- Pustilnik, S. A., Kniazev, A. Y., & Pramskij, A. G. 2005, *A&A*, 443, 91
- Raimann, D., Storch-Bergmann, T., Bica, E., Melnick, J., & Schmitt, H. 2000, *MNRAS*, 316, 559
- Rayo, J. F., Peimbert, M., & Torres-Peimbert, S. 1982, *ApJ*, 255, 1
- Rieke, G. H., & Lebofsky, M. J. 1979, *ARA&A*, 17, 477
- 1985, *ApJ*, 288, 618
- Roche, P. F., Aitken, D. K., Smith, C. H., & Ward, M. J. 1991, *MNRAS*, 248, 606
- Rosenberg, J. L., Wu, Y., Le Floch, E., Charmandaris, V., Ashby, M. L. N., Houck, J. R., Salzer, J. J., & Willner, S. P. 2008, *ApJ*, 674, 814
- Rosolowsky, E., & Simon, J. D. 2008, *ApJ*, 675, 1213
- Roy, J.-R., Belley, J., Dutil, Y., & Martin, P. 1996, *ApJ*, 460, 284
- Russell, S. C., & Dopita, M. A. 1990, *ApJS*, 74, 93
- Ryder, S. D. 1995, *ApJ*, 444, 610
- Sabbadin, F., Ortolani, S., & Bianchini, A. 1984, *A&A*, 131, 1
- Saviane, I., Ivanov, V. D., Held, E. V., Alloin, D., Rich, R. M., Bresolin, F., & Rizzi, L. 2008, *A&A*, 487, 901
- Schlegel, D. J., Finkbeiner, D. P., & Davis, M. 1998, *ApJ*, 500, 525
- Shi, F., Kong, X., Li, C., & Cheng, F. Z. 2005, *A&A*, 437, 849
- Skillman, E. D. 1985, *ApJ*, 290, 449
- Skillman, E. D., Bomans, D. J., & Kobulnicky, H. A. 1997, *ApJ*, 474, 205
- Skillman, E. D., Côté, S., & Miller, B. W. 2003, *AJ*, 125, 610
- Skillman, E. D., Kennicutt, R. C., & Hodge, P. W. 1989a, *ApJ*, 347, 875
- Skillman, E. D., Terlevich, R. J., Kennicutt, Jr., R. C., Garnett, D. R., & Terlevich, E. 1994, *ApJ*, 431, 172
- Skillman, E. D., Terlevich, R., & Melnick, J. 1989b, *MNRAS*, 240, 563
- Skrutskie, M. F., et al. 2003, *VizieR Online Data Catalog*, 7233, 0
- 2006, *AJ*, 131, 1163
- Smith, H. E. 1975, *ApJ*, 199, 591
- Smith, J. D. T., et al. 2007a, *PASP*, 119, 1133
- 2007b, *ApJ*, 656, 770
- Stasińska, G., Comte, G., & Vigroux, L. 1986, *A&A*, 154, 352

- Storchi-Bergmann, T., Calzetti, D., & Kinney, A. L. 1994, *ApJ*, 429, 572
- Talent, D. L. 1983, *PASP*, 95, 986
- Thuan, T. X., & Izotov, Y. I. 2005, *ApJS*, 161, 240
- Thuan, T. X., Sauvage, M., & Madden, S. 1999, *ApJ*, 516, 783
- Torres-Peimbert, S., Peimbert, M., & Fierro, J. 1989, *ApJ*, 345, 186
- Tüllmann, R., Rosa, M. R., Elwert, T., Bomans, D. J., Ferguson, A. M. N., & Dettmar, R.-J. 2003, *A&A*, 412, 69
- Vaduvescu, O., McCall, M. L., & Richer, M. G. 2007, *AJ*, 134, 604
- van Driel, W., Kraan-Korteweg, R. C., Binggeli, B., & Huchtmeier, W. K. 1998, *A&AS*, 127, 397
- van Zee, L. 2000, *ApJ*, 543, L31
- van Zee, L., & Haynes, M. P. 2006, *ApJ*, 636, 214
- van Zee, L., Haynes, M. P., & Salzer, J. J. 1997a, *AJ*, 114, 2497
- . 1997b, *AJ*, 114, 2479
- van Zee, L., Salzer, J. J., Haynes, M. P., O'Donoghue, A. A., & Balonek, T. J. 1998, *AJ*, 116, 2805
- van Zee, L., Skillman, E. D., & Haynes, M. P. 2006, *ApJ*, 637, 269
- Vázquez, G. A., & Leitherer, C. 2005, *ApJ*, 621, 695
- Vermeij, R., & van der Hulst, J. M. 2002, *A&A*, 391, 1081
- Vila Costas, M. B., & Edmunds, M. G. 1993, *MNRAS*, 265, 199
- Vilchez, J. M., Edmunds, M. G., & Pagel, B. E. J. 1988a, *PASP*, 100, 1428
- Vilchez, J. M., Pagel, B. E. J., Diaz, A. I., Terlevich, E., & Edmunds, M. G. 1988b, *MNRAS*, 235, 633
- Walsh, J. R., & Roy, J.-R. 1989, *MNRAS*, 239, 297
- . 1997, *MNRAS*, 288, 726
- Webster, B. L., Longmore, A. J., Hawarden, T. G., & Mebold, U. 1983, *MNRAS*, 205, 643
- Webster, B. L., & Smith, M. G. 1983, *MNRAS*, 204, 743
- Welch, G. A. 1970, *ApJ*, 161, 821
- Werner, M. W., et al. 2004, *ApJS*, 154, 1
- Whiting, A. B., Hau, G. K. T., Irwin, M., & Verdugo, M. 2007, *AJ*, 133, 715
- Wu, R., Hogg, D. W., & Moustakas, J. 2009, *ArXiv e-prints*
- Wu, Y., Charmandaris, V., Hao, L., Brandl, B. R., Bernard-Salas, J., Spoon, H. W. W., & Houck, J. R. 2006, *ApJ*, 639, 157
- Wu, Y., et al. 2007, *ApJ*, 662, 952
- Zamorano, J., & Rego, M. 1986, *A&A*, 170, 31
- Zaritsky, D., Kennicutt, Jr., R. C., & Huchra, J. P. 1994, *ApJ*, 420, 87

TABLE 1
GALAXIES.

Galaxy	Coordinates			Distance			Oxygen Abundance			Subsample	
	α (J2000.0)	δ (J2000.0)	Ref.	cz (km/s)	D (Mpc)	Ref.	$12+\text{Log}_{10}(\text{O}/\text{H})$	Method ^a	Ref.	LVL	IRS
WLM	00:01:58.1	-15:27:39	1	-116	0.92	1	7.77 ± 0.10	$\lambda 4363$	2-5	✓	...
NGC 0024	00:09:56.7	-24:57:44	1	554	8.13	1	✓	...
NGC 0045	00:14:04.0	-23:10:55	1	471	7.07	1	✓	...
NGC 0055	00:14:54.0	-39:11:49	1	129	2.17	1	8.36 ± 0.10	strong	6-10	✓	...
NGC 0059	00:15:25.4	-21:26:42	1	382	5.30	1	8.40 ± 0.11	$\lambda 4363$	11	✓	...
ESO 410-G005	00:15:31.4	-32:10:48	12	...	1.90	12	✓	...
Sculptor-dE1	00:23:51.7	-24:42:18	12	...	4.20	12	✓	...
ESO 294-G010	00:26:33.3	-41:51:20	12	117	1.90	12	✓	...
IC 1574	00:43:03.8	-22:14:49	1	361	4.92	1	✓	...
NGC 0247	00:47:08.3	-20:45:38	1	160	3.65	1	✓	...
NGC 0253	00:47:33.1	-25:17:18	1	241	3.94	1	8.99 ± 0.31	strong	6,9,13	✓	...
ESO 540-G030	00:49:21.1	-18:04:28	12	...	3.40	12	✓	...
UGCA 015	00:49:49.2	-21:00:54	1	301	3.34	1	✓	...
ESO 540-G032	00:50:24.6	-19:54:25	12	...	3.40	12	✓	...
UGC 00521	00:51:12.2	+12:01:31	14	659	11.32	15,16	7.86 ± 0.04	$\lambda 4363$	17,18	✓	...
SMC	00:52:44.8	-72:49:43	1	158	0.06	1	7.96 ± 0.15	$\lambda 4363$	19,20	✓	...
NGC 0300	00:54:53.5	-37:41:00	1	144	2.00	1	8.73 ± 0.04	mix	6,9,13,21,22	✓	...
NGC 0337	00:59:50.3	-07:34:44	23	1650	24.70	23	✓	✓
UGC 00668	01:04:47.8	+02:07:04	1	-234	0.65	1	7.62 ± 0.05	$\lambda 4363$	24-26	✓	...
UGC 00685	01:07:22.4	+16:41:02	1	157	4.70	1	8.00 ± 0.03	$\lambda 4363$	27,28	✓	...
UGC 00695	01:07:46.4	+01:03:49	1	664	10.20	1	✓	...
NGC 0404	01:09:26.9	+35:43:03	12	-48	3.10	12	✓	...
UGC 00891	01:21:18.9	+12:24:43	1	643	10.84	1	8.20 ± 0.10	strong	17,18	✓	...
UGC 01056	01:28:47.3	+16:41:19	1	595	10.32	1	✓	...
NGC 0584	01:31:20.7	-06:52:05	23	1854	27.60	23	✓	✓
UGC 01104	01:32:42.5	+18:19:02	1	686	7.50	1	7.94 ± 0.05	$\lambda 4363$	28,29	✓	...
NGC 0598	01:33:50.9	+30:39:37	1	-179	0.84	1	8.36 ± 0.05	mix	9,24,30-35	✓	...
NGC 0625	01:35:04.2	-41:26:15	1	405	4.07	1	8.08 ± 0.12	$\lambda 4363$	11,36	✓	...
NGC 0628	01:36:41.7	+15:46:59	1	657	7.30	1	9.06 ± 0.10	mix	9,13,30,37-41	✓	✓
UGC 01176	01:40:09.9	+15:54:17	1	633	9.00	1	✓	...
ESO 245-G005	01:45:03.7	-43:35:53	1	395	4.43	1	7.70 ± 0.10	$\lambda 4363$	11,42,43	✓	...
UGC 01249	01:47:30.6	+27:19:52	1	338	7.20	1	8.62 ± 0.20	strong	27	✓	...
NGC 0672	01:47:54.3	+27:25:59	1	421	7.20	1	✓	...
ESO 245-G007	01:51:06.3	-44:26:41	1	56	0.44	1	✓	...
NGC 0784	02:01:17.0	+28:50:15	1	198	5.19	1	7.88 ± 0.20	strong	27,44	✓	...
NGC 0855	02:14:03.6	+27:52:38	1	595	9.73	1	✓	...
ESO 115-G021	02:37:48.1	-61:20:18	1	513	4.99	1	✓	...
NGC 1097	02:46:19.0	-30:16:30	23	1275	16.90	23	✓	✓
ESO 154-G023	02:56:50.4	-54:34:17	1	578	5.76	1	✓	...
NGC 1291	03:17:18.3	-41:06:28	1	839	9.37	1	✓	...
NGC 1313	03:18:15.8	-66:29:53	1	475	4.15	1	8.41 ± 0.09	strong	9,45-47	✓	...
NGC 1311	03:20:07.4	-52:11:07	1	571	5.45	1	✓	...
NGC 1316	03:22:41.7	-37:12:30	23	1760	26.30	23	✓	✓
UGC 02716	03:24:07.2	+17:45:12	1	379	6.23	1	✓	...
IC 1959	03:33:11.8	-50:24:38	1	640	6.06	1	✓	...
NGC 1482	03:54:39.3	-20:30:09	23	1655	22.00	23	✓	✓
NGC 1487	03:55:46.1	-42:22:05	1	848	9.08	1	8.19 ± 0.20	strong	48,49	✓	...
NGC 1510	04:03:32.6	-43:24:00	1	913	9.84	1	8.38 ± 0.20	strong	46,49,50	✓	...
NGC 1512	04:03:54.3	-43:20:57	1	896	9.64	1	✓	✓
NGC 1522	04:06:07.7	-52:40:09	1	905	9.32	1	8.20 ± 0.12	$\lambda 4363$	51	✓	...
IC 2049	04:12:04.3	-58:33:25	52	1469 ^b	16.73	15,16	✓	...
ESO 483-G013	04:12:41.3	-23:09:36	1	823	10.43	1	✓	...
NGC 1566	04:20:00.4	-54:56:16	23	1496	18.00	23	✓	✓
ESO 158-G003	04:46:16.7	-57:20:35	1	975	9.96	1	✓	...
ESO 119-G016	04:51:29.2	-61:39:03	1	969	9.84	1	✓	...
NGC 1705	04:54:13.7	-53:21:41	1	628	5.10	1	8.21 ± 0.05	$\lambda 4363$	46,53,54	✓	...
NGC 1744	04:59:57.6	-26:01:19	1	748	7.65	1	✓	...
NGC 1796	05:02:42.8	-61:08:23	1	987	10.32	1	✓	...
ESO 486-G021	05:03:19.7	-25:25:23	1	865	8.89	1	✓	...
MCG -05-13-004	05:06:24.1	-31:57:11	1	686	6.63	1	✓	...
NGC 1800	05:06:25.4	-31:57:15	1	803	8.24	1	8.36 ± 0.20	strong	27,46,55	✓	...
UGCA 106	05:11:59.3	-32:58:21	1	933	9.77	1	✓	...
LMC	05:23:34.5	-69:45:22	1	278	0.05	1	8.26 ± 0.15	$\lambda 4363$	19,20	✓	...
KKH 037	06:47:45.8	+80:07:26	1	-148	3.39	1	✓	...
NGC 2366	07:28:54.6	+69:12:57	1	100	3.19	1	7.91 ± 0.05	$\lambda 4363$	4,11,38,44,56-61	✓	...
UGCA 133	07:34:11.5	+66:52:47	62	...	3.20	12	✓	...
NGC 2403	07:36:51.4	+65:36:09	1	131	3.22	1	8.39 ± 0.10	mix	9,13,24,30,32,38,40,63	✓	✓
NGC 2500	08:01:53.3	+50:44:15	1	514	7.63	1	8.75 ± 0.20	strong	27	✓	...
NGC 2537	08:13:13.2	+45:59:41	64	447	6.90	1	8.44 ± 0.20	strong	27,64-66	✓	...
UGC 04278	08:13:58.9	+45:44:34	1	565	7.59	1	8.08 ± 0.19	$\lambda 4363$	67,68	✓	...
UGC 04305	08:19:04.0	+70:43:09	1	157	3.39	1	7.92 ± 0.10	$\lambda 4363$	4,38,44,69,70	✓	...
NGC 2552	08:19:20.1	+50:00:25	1	524	7.65	1	8.39 ± 0.17	strong	4,27,68	✓	...
M81dwA	08:23:56.0	+71:01:45	1	113	3.55	1	✓	...
UGC 04426	08:28:28.4	+41:51:24	1	397	10.28	1	✓	...
UGC 04459	08:34:07.2	+66:10:54	1	19	3.56	1	7.82 ± 0.09	$\lambda 4363$	4,11,27,44,70-72	✓	...
UGC 04483	08:37:03.0	+69:46:51	64	178	3.21	1	7.56 ± 0.03	$\lambda 4363$	11,27,28,73	✓	...
NGC 2683	08:52:41.4	+33:25:14	1	411	7.70	1	✓	...

TABLE 1 — *Continued*

Galaxy	Coordinates			Distance			Oxygen Abundance			Subsample	
	α (J2000.0)	δ (J2000.0)	Ref.	cz (km/s)	D (Mpc)	Ref.	$12+\text{Log}_{10}(\text{O}/\text{H})$	Method ^a	Ref.	LVL	IRS
UGC 04704	08:59:00.3	+39:12:36	1	596	7.75	1	✓	...
UGC 04787	09:07:34.9	+33:16:36	1	552	6.53	1	8.19 ± 0.20	strong	27,29	✓	...
NGC 2798	09:17:22.9	+41:59:59	23	1726	24.70	23	✓
NGC 2841	09:22:02.6	+50:58:35	23	638	9.80	23	✓
UGC 04998	09:25:12.1	+68:22:59	1	623	10.50	1	✓	...
NGC 2903	09:32:10.2	+21:30:06	64	556	8.90	1	8.90 ± 0.10	mix	9,13,24,27,30,40,74,75	✓	...
UGC 05076	09:32:36.4	+51:52:19	1	571	8.31	1	✓	...
CGCG 035–007	09:34:44.9	+06:25:32	1	574	5.17	1	✓	...
UGC 05139	09:40:32.3	+71:10:56	1	143	3.84	1	8.00 ± 0.10	$\lambda 4363$	70,76	✓	...
IC 0559	09:44:43.9	+09:36:55	1	513	4.93	1	✓	...
F8D1	09:44:47.1	+67:26:19	12	...	3.80	12	✓	...
[FM2000] 1	09:45:10.0	+68:45:54	77	...	3.40	15,16	✓	...
NGC 2976	09:47:15.3	+67:55:00	1	3	3.56	1	✓	✓
LEDA 166101	09:50:10.0	+67:30:24	12	...	3.50	12	✓	...
UGC 05272	09:50:22.4	+31:29:16	1	520	7.10	1	7.83 ± 0.08	$\lambda 4363$	44,78,79	✓	...
UGC 05288	09:51:17.0	+07:49:39	1	557	6.80	1	7.90 ± 0.03	$\lambda 4363$	28	✓	...
BK 03N	09:53:48.5	+68:58:08	1	-40	4.02	1	✓	...
NGC 3049	09:54:49.6	+09:16:18	23	1494	19.60	23	✓
NGC 3031	09:55:33.2	+69:03:55	1	-34	3.63	1	9.00 ± 0.13	mix	9,13,24,32,80,81	✓	...
NGC 3034	09:55:52.2	+69:40:47	1	203	3.53	1	9.31 ± 0.50	$\lambda 4363$	80	✓	...
UGC 05340	09:56:45.7	+28:49:35	1	503	5.90	1	7.21 ± 0.03	$\lambda 4363$	44,82	✓	...
KDG 061	09:57:03.1	+68:35:31	1	-135	3.60	1	8.35 ± 0.05^c	$\lambda 4363$	70,83	✓	...
UGC 05336	09:57:32.0	+69:02:45	1	46	3.70	1	8.65 ± 0.25^c	strong	70	✓	...
Arp's Loop	09:57:32.6	+69:16:60	84	99	3.90	15,16	✓	...
UGC 05364	09:59:26.4	+30:44:47	1	20	0.69	1	7.30 ± 0.05	PN	71,85	✓	...
UGC 05373	10:00:00.1	+05:19:56	1	301	1.44	1	7.84 ± 0.05	$\lambda 4363$	4,5,8,71,86–89	✓	...
KKH 057	10:00:16.0	+63:11:06	12	...	3.90	12	✓	...
UGCA 193	10:02:36.0	-06:00:49	1	662	9.70	1	✓	...
NGC 3109	10:03:06.6	-26:09:32	1	403	1.34	1	7.77 ± 0.07	$\lambda 4363$	44,69,89,90	✓	...
NGC 3077	10:03:19.1	+68:44:01	64	14	3.82	1	8.64 ± 0.20	strong	27,46,64	✓	...
AM 1001–270	10:04:04.0	-27:19:55	12	362	1.30	12	✓	...
BK 05N	10:04:41.4	+68:15:23	91	...	3.80	12	✓	...
UGC 05428	10:05:06.4	+66:33:32	1	-129	3.50	1	✓	...
UGC 05423	10:05:30.6	+70:21:52	1	350	5.30	1	7.98 ± 0.10	$\lambda 4363$	27,76	✓	...
UGC 05442	10:07:01.9	+67:49:39	1	-18	3.70	1	✓	...
UGC 05456	10:07:19.6	+10:21:46	1	544	3.80	1	✓	...
IKN	10:08:05.9	+68:23:57	12	...	3.70	12	✓	...
Sextans A	10:11:00.8	-04:41:34	1	324	1.32	1	7.54 ± 0.09	$\lambda 4363$	5,59,71,87,88	✓	...
NGC 3190	10:18:05.6	+21:49:55	23	1271	17.40	23	✓
NGC 3184	10:18:17.0	+41:25:28	23	592	8.60	23	✓
[HS98] 117	10:21:25.2	+71:06:58	12	-37	4.00	12	✓	...
NGC 3239	10:25:05.6	+17:09:37	1	753	8.29	1	8.60 ± 0.20	strong	27	✓	...
DDO 078	10:26:28.0	+67:39:35	62	55	3.70	12	✓	...
UGC 05672	10:28:20.9	+22:34:17	1	531	6.30	1	✓	...
UGC 05666	10:28:21.2	+68:24:43	1	57	4.02	1	7.93 ± 0.05	$\lambda 4363$	38,70,76	✓	...
UGC 05692	10:30:35.0	+70:37:07	1	180	4.00	1	7.95 ± 0.20	strong	70	✓	...
NGC 3265	10:31:06.8	+28:47:47	23	1421	20.00	23	✓
NGC 3274	10:32:17.1	+27:40:07	1	537	6.50	1	8.01 ± 0.20	strong	4,27,55	✓	...
MRK 0033	10:32:31.9	+54:24:03	23	1461	21.70	23	✓
BK 06N	10:34:29.0	+66:00:30	62	...	3.80	12	✓	...
NGC 3299	10:36:23.8	+12:42:27	1	641	10.40	1	✓	...
UGC 05764	10:36:43.3	+31:32:48	1	586	7.08	1	7.95 ± 0.04	$\lambda 4363$	17,18,44	✓	...
UGC 05797	10:39:25.2	+01:43:05	1	713	6.84	1	✓	...
UGC 05829	10:42:42.2	+34:26:56	1	629	7.88	1	8.30 ± 0.10	strong	17,18	✓	...
NGC 3344	10:43:30.9	+24:55:22	1	586	6.64	1	8.76 ± 0.02	strong	9,30,75,92,93	✓	...
NGC 3351	10:43:57.7	+11:42:13	1	778	10.00	1	9.09 ± 0.01	strong	30,32,75,94–96	✓	✓
NGC 3368	10:46:45.7	+11:49:12	1	897	10.52	1	9.04 ± 0.20	strong	32,94,95	✓	...
UGC 05889	10:47:22.3	+14:04:10	1	572	9.30	1	✓	...
UGC 05923	10:49:07.6	+06:55:02	1	712	7.16	1	8.26 ± 0.20	strong	29	✓	...
UGC 05918	10:49:36.5	+65:31:50	1	340	7.40	1	7.84 ± 0.04	$\lambda 4363$	70	✓	...
NGC 3432	10:52:31.3	+36:37:11	1	616	7.89	1	8.65 ± 0.20	strong	27	✓	...
KDG 073	10:52:57.1	+69:32:58	1	-132	3.70	1	✓	...
NGC 3486	11:00:23.9	+28:58:30	1	681	8.24	1	✓	...
NGC 3510	11:03:43.4	+28:53:13	1	705	8.57	1	8.08 ± 0.20	strong	27,29,55	✓	...
NGC 3521	11:05:48.6	-00:02:09	1	805	8.03	1	8.83 ± 0.03	strong	9,75	✓	✓
NGC 3593	11:14:37.0	+12:49:04	1	628	6.52	1	✓	...
NGC 3623	11:18:55.9	+13:05:37	1	807	8.95	1	9.06 ± 0.20	strong	32,94	✓	...
NGC 3627	11:20:15.0	+12:59:30	1	727	10.05	1	9.13 ± 0.20	strong	97	✓	✓
NGC 3628	11:20:17.0	+13:35:20	64	843	9.45	1	9.02 ± 0.20	strong	27,64	✓	...
UGC 06457	11:27:12.2	-00:59:41	1	963	10.24	1	✓	...
UGC 06541	11:33:28.9	+49:14:22	64	249	3.89	1	7.82 ± 0.06	$\lambda 4363$	27,60,61,68,98–102	✓	...
NGC 3738	11:35:48.8	+54:31:26	1	229	4.90	1	8.23 ± 0.01	$\lambda 4363$	4,27,55,59	✓	...
NGC 3741	11:36:06.2	+45:17:01	1	229	3.19	1	7.62 ± 0.20	strong	27,103	✓	...
NGC 3773	11:38:13.0	+12:06:43	23	987	12.90	23	✓
UGC 06782	11:48:57.4	+23:50:15	91	525	14.00	15,16	✓	...
UGC 06817	11:50:53.0	+38:52:49	1	242	2.64	1	✓	...
UGC 06900	11:55:39.4	+31:31:10	1	590	7.47	1	8.10 ± 0.30	strong	4	✓	...
NGC 4020	11:58:56.6	+30:24:44	1	760	9.68	1	8.73 ± 0.20	strong	27	✓	...

TABLE 1 — *Continued*

Galaxy	Coordinates			Distance			Oxygen Abundance			Subsample	
	α (J2000.0)	δ (J2000.0)	Ref.	cz (km/s)	D (Mpc)	Ref.	12+Log ₁₀ (O/H)	Method ^a	Ref.	LVL	IRS
NGC 4068	12:04:00.8	+52:35:18	1	210	4.31	1	7.84 ± 0.20	strong	27	✓	...
NGC 4080	12:04:51.8	+26:59:33	1	567	6.92	1	✓	...
NGC 4096	12:06:01.0	+47:28:40	1	566	8.28	1	8.78 ± 0.20	strong	27	✓	...
NGC 4125	12:08:06.0	+65:10:27	23	1356	21.40	23	✓	✓
NGC 4144	12:09:58.4	+46:27:27	1	265	9.80	1	8.65 ± 0.20	strong	27	✓	...
NGC 4163	12:12:09.1	+36:10:09	1	165	2.96	1	7.91 ± 0.20	strong	27	✓	...
NGC 4190	12:13:44.7	+36:38:03	1	228	3.50	1	7.93 ± 0.20	strong	27	✓	...
ESO 321-G014	12:13:49.6	-38:13:53	12	610	3.20	12	✓	...
UGC 07242	12:14:08.4	+66:05:41	1	68	5.42	1	✓	...
UGCA 276	12:14:57.9	+36:13:08	1	284	3.18	1	✓	...
UGC 07267	12:15:23.6	+51:20:58	1	472	7.33	1	✓	...
NGC 4214	12:15:39.5	+36:19:35	64	291	2.92	1	8.25 ± 0.10	λ4363	4,27,38,55,59,60,104,105	✓	...
CGCG 269-049	12:15:46.8	+52:23:17	1	159	3.23	1	7.43 ± 0.06	λ4363	106	✓	...
NGC 4236	12:16:42.1	+69:27:46	1	0	4.45	1	8.32 ± 0.20	strong	107	✓	...
NGC 4244	12:17:29.9	+37:48:29	1	244	4.49	1	8.80 ± 0.20	strong	27	✓	...
NGC 4242	12:17:30.1	+45:37:08	1	517	7.43	1	✓	...
UGC 07321	12:17:34.0	+22:32:25	91	408	20.00	15,16	✓	...
NGC 4248	12:17:50.3	+47:24:31	1	484	7.24	1	8.15 ± 0.20	strong	27,29	✓	...
NGC 4254	12:18:49.6	+14:24:59	23	2407	20.00	23	✓	✓
NGC 4258	12:18:57.5	+47:18:14	1	448	7.98	1	8.89 ± 0.20	strong	9,32,94,95,108	✓	...
I SZ 399	12:19:59.5	-17:23:31	1	900	8.97	1	✓	...
NGC 4288	12:20:38.1	+46:17:33	1	535	7.67	1	8.52 ± 0.20	strong	27,29	✓	...
UGC 07408	12:21:15.0	+45:48:41	1	462	6.87	1	✓	...
NGC 4321	12:22:54.9	+15:49:21	23	1571	20.00	23	✓	✓
UGC 07490	12:24:25.3	+70:20:01	1	465	8.40	1	8.46 ± 0.20	strong	4	✓	...
NGC 4395	12:25:48.9	+33:32:48	1	319	4.61	1	8.35 ± 0.20	strong	30,40,58,109	✓	...
UGCA 281	12:26:16.0	+48:29:37	1	281	5.70	1	7.80 ± 0.03	λ4363	27,61,110-112	✓	...
UGC 07559	12:27:05.1	+37:08:33	1	218	4.87	1	✓	...
UGC 07577	12:27:40.9	+43:29:44	1	196	2.74	1	✓	...
NGC 4449	12:28:11.1	+44:05:37	64	207	4.21	1	8.31 ± 0.07	λ4363	30,55,59,68,105,113	✓	...
UGC 07599	12:28:28.5	+37:14:01	1	278	6.90	1	✓	...
UGC 07605	12:28:38.7	+35:43:03	1	309	4.43	1	✓	...
NGC 4455	12:28:44.1	+22:49:21	1	637	7.75	1	7.99 ± 0.20	strong	27	✓	...
UGC 07608	12:28:45.3	+43:13:35	1	538	7.76	1	✓	...
NGC 4460	12:28:45.5	+44:51:51	1	490	9.59	1	✓	...
UGC 07639	12:29:53.4	+47:31:52	1	382	8.00	1	✓	...
NGC 4485	12:30:31.1	+41:42:01	1	493	7.07	1	✓	...
NGC 4490	12:30:36.1	+41:38:34	1	565	8.03	1	✓	...
UGC 07690	12:32:26.8	+42:42:18	1	537	7.73	1	7.97 ± 0.20	strong	27	✓	...
UGC 07699	12:32:48.0	+37:37:18	1	496	6.85	1	8.15 ± 0.20	strong	29	✓	...
UGC 07698	12:32:54.4	+31:32:28	1	331	6.10	1	8.04 ± 0.20	strong	4	✓	...
UGC 07719	12:34:00.6	+39:01:10	1	678	9.39	1	✓	...
NGC 4536	12:34:27.1	+02:11:16	23	1808	25.00	23	✓	✓
NGC 4559	12:35:57.7	+27:57:35	23	816	11.60	23	✓	✓
UGC 07774	12:36:22.5	+40:00:19	1	526	7.44	1	✓	...
UGCA 292	12:38:39.8	+32:45:52	64	307	3.10	1	7.30 ± 0.03	λ4363	28,114	✓	...
NGC 4594	12:39:59.4	-11:37:23	1	1024	9.33	1	✓	...
NGC 4605	12:40:00.3	+61:36:29	1	143	5.47	1	8.64 ± 0.20	strong	27	✓	...
NGC 4618	12:41:32.7	+41:09:04	1	544	7.79	1	8.70 ± 0.20	strong	27	✓	...
NGC 4625	12:41:52.6	+41:16:26	1	609	8.65	1	8.44 ± 0.20	strong	27,115	✓	✓
NGC 4631	12:42:08.0	+32:32:26	1	606	8.05	1	✓	✓
UGC 07866	12:42:15.1	+38:30:12	1	354	4.57	1	✓	...
NGC 4656	12:43:57.7	+32:10:05	1	646	8.59	1	7.93 ± 0.20	strong	27,107	✓	...
UGC 07916	12:44:25.1	+34:23:12	1	607	8.21	1	✓	...
UGC 07950	12:46:56.4	+51:36:46	1	502	7.91	1	8.37 ± 0.10	λ4363	4,27,29,112	✓	...
UGC 07949	12:46:59.8	+36:28:35	1	333	9.90	1	✓	...
NGC 4707	12:48:22.9	+51:09:53	1	468	7.44	1	8.43 ± 0.20	strong	4	✓	...
NGC 4736	12:50:53.0	+41:07:14	1	308	4.66	1	9.01 ± 0.17	strong	9,27,30,32,75,94,116	✓	✓
UGC 08024	12:54:05.2	+27:08:55	1	374	4.30	1	7.67 ± 0.06	λ4363	17,117	✓	...
NGC 4826	12:56:43.7	+21:40:52	1	408	7.50	1	9.09 ± 0.20	strong	94	✓	✓
UGC 08091	12:58:40.4	+14:13:03	1	214	2.13	1	7.65 ± 0.06	λ4363	8,44,85,86,118	✓	...
UGCA 319	13:02:14.4	-17:14:15	1	747	7.40	1	✓	...
UGCA 320	13:03:16.8	-17:25:23	1	744	7.24	1	8.08 ± 0.20	strong	26,27	✓	...
UGC 08188	13:05:49.5	+37:36:18	1	321	4.49	1	✓	...
UGC 08201	13:06:24.8	+67:42:25	1	37	4.57	1	7.80 ± 0.20	strong	70	✓	...
MCG -03-34-002	13:07:56.6	-16:41:21	1	922	10.16	1	✓	...
UGC 08245	13:08:34.2	+78:56:13	1	70	3.64	1	✓	...
NGC 5023	13:12:12.1	+44:02:20	1	407	5.40	1	✓	...
CGCG 217-018	13:12:51.8	+40:32:35	1	570	8.21	1	✓	...
NGC 5033	13:13:27.5	+36:35:38	23	875	13.30	23	✓	✓
UGC 08313	13:13:54.1	+42:12:36	1	625	8.72	1	✓	...
UGC 08320	13:14:27.9	+45:55:09	1	192	4.33	1	8.29 ± 0.20	strong	4,118	✓	...
UGC 08331	13:15:30.3	+47:29:56	1	260	8.20	1	✓	...
NGC 5055	13:15:49.2	+42:01:49	1	504	7.55	1	9.21 ± 0.20	strong	9,13,30	✓	✓
NGC 5068	13:18:54.6	-21:02:20	1	673	6.24	1	8.82 ± 0.22	strong	30,119	✓	...
IC 4247	13:26:44.4	-30:21:45	1	274	4.97	1	8.27 ± 0.20	strong	89	✓	...
NGC 5204	13:29:36.2	+58:25:06	1	201	4.65	1	✓	...
NGC 5194	13:29:52.7	+47:11:43	1	463	8.00	1	9.04 ± 0.01	strong	9,13,24,27,30,32,75,120-122	✓	✓

TABLE 1 — *Continued*

Galaxy	Coordinates			Distance			Oxygen Abundance			Subsample	
	α (J2000.0)	δ (J2000.0)	Ref.	c_z (km/s)	D (Mpc)	Ref.	12+Log ₁₀ (O/H)	Method ^a	Ref.	LVL	IRS
NGC 5195	13:29:58.7	+47:16:05	1	465	8.00	1	✓	✓
UGC 08508	13:30:44.4	+54:54:36	1	62	2.69	1	7.89 ± 0.20	strong	27,123	✓	...
NGC 5229	13:34:02.7	+47:54:55	1	364	5.10	1	✓	...
NGC 5238	13:34:42.7	+51:36:51	1	235	5.20	1	7.96 ± 0.20	strong	27	✓	...
[KK98] 208	13:36:35.5	-29:34:17	1	381	4.68	1	✓	...
NGC 5236	13:37:00.6	-29:51:57	64	516	4.47	1	9.16 ± 0.12	strong	6,9,13,46,74,96,115,124	✓	...
ESO 444-G084	13:37:20.1	-28:02:46	1	587	4.61	1	7.45 ± 0.20	strong	26	✓	...
UGC 08638	13:39:19.4	+24:46:32	1	274	4.27	1	✓	...
UGC 08651	13:39:53.8	+40:44:21	1	201	3.02	1	7.85 ± 0.04	λ4363	28	✓	...
NGC 5253	13:39:56.0	-31:38:24	64	404	3.15	1	8.15 ± 0.10	λ4363	6,27,46,55,59,105,125-128	✓	...
NGC 5264	13:41:36.9	-29:54:50	1	478	4.53	1	8.66 ± 0.20	strong	26,27	✓	...
UGC 08760	13:50:50.6	+38:01:09	1	193	3.24	1	✓	...
KKH 086	13:54:33.6	+04:14:35	12	287	2.60	12	✓	...
UGC 08837	13:54:45.7	+53:54:03	1	144	8.30	1	7.70 ± 0.30	λ4363	129	✓	...
UGC 08833	13:54:48.7	+35:50:15	1	228	3.20	1	✓	...
NGC 5457	14:03:12.5	+54:20:55	1	241	6.70	1	8.68 ± 0.10	mix	9,13,24,30,40,109,130-137	✓	...
NGC 5474	14:05:01.5	+53:39:45	1	273	7.20	1	✓	...
NGC 5477	14:05:33.1	+54:27:39	1	304	7.70	1	8.14 ± 0.07	λ4363	138	✓	...
[KK98] 230	14:07:10.5	+35:03:37	1	62	2.14	1	✓	...
UGC 09128	14:15:57.2	+23:03:22	64	154	2.24	1	7.75 ± 0.05	λ4363	17,18,71	✓	...
NGC 5585	14:19:48.2	+56:43:46	1	305	5.70	1	✓	...
UGC 09240	14:24:43.4	+44:31:33	1	150	2.80	1	7.95 ± 0.03	λ4363	27,28,118	✓	...
UGC 09405	14:35:24.4	+57:15:19	1	222	8.00	1	✓	...
MRK 0475	14:39:05.4	+36:48:21	1	583	9.02	1	7.97 ± 0.02	λ4363	60,139	✓	...
NGC 5713	14:40:11.5	-00:17:21	23	1883	26.60	23	✓	✓
NGC 5832	14:57:45.7	+71:40:56	1	447	8.74	1	✓	...
NGC 5866	15:06:29.5	+55:45:48	23	692	12.50	23	✓	✓
NGC 5949	15:28:00.7	+64:45:47	1	435	8.53	1	✓	...
UGC 09992	15:41:47.8	+67:15:15	1	427	8.56	1	7.88 ± 0.12	λ4363	28	✓	...
KKR 25	16:13:47.6	+54:22:16	12	-139	1.90	12	✓	...
NGC 6503	17:49:27.1	+70:08:40	1	60	5.27	1	✓	...
IC 4951	20:09:31.2	-61:50:47	1	794	9.34	1	✓	...
NGC 6946	20:34:52.3	+60:09:14	23	48	5.50	23	✓	✓
DDO 210	20:46:51.8	-12:50:53	1	-137	0.94	1	✓	...
IC 5052	20:52:06.3	-69:12:13	1	598	5.86	1	✓	...
NGC 7064	21:29:03.0	-52:46:03	1	797	9.86	1	✓	...
NGC 7090	21:36:28.6	-54:33:24	1	857	10.41	1	✓	...
IC 5152	22:02:41.9	-51:17:44	1	124	1.97	1	7.92 ± 0.07	λ4363	26,118,140	✓	...
NGC 7331	22:37:04.1	+34:24:56	23	816	15.70	23	✓	✓
IC 5256	22:49:45.8	-68:41:26	1	950	10.76	1	✓	...
NGC 7552	23:16:11.0	-42:34:59	23	1585	22.30	23	✓	✓
UGCA 438	23:26:27.5	-32:23:20	1	62	2.22	1	✓	...
ESO 347-G017	23:26:56.0	-37:20:49	1	690	9.37	1	7.90 ± 0.09	λ4363	11,26,36	✓	...
UGC 12613	23:28:36.2	+14:44:35	1	-183	0.76	1	7.93 ± 0.14	strong	141	✓	...
IC 5332	23:34:27.4	-36:06:05	1	706	9.53	1	✓	...
NGC 7713	23:36:15.4	-37:56:19	1	689	9.28	1	8.69 ± 0.20	strong	27	✓	...
UGCA 442	23:43:45.5	-31:57:22	1	267	4.27	1	7.72 ± 0.03	λ4363	26,36,42	✓	...
KKH 098	23:45:34.0	+38:43:04	12	-137	2.50	12	✓	...
ESO 149-G003	23:52:02.8	-52:34:40	1	594	6.40	1	✓	...
NGC 7793	23:57:49.7	-32:35:30	1	230	3.91	1	8.82 ± 0.07	mix	6,9,13,30,46,142,143	✓	✓

REFERENCES. — (1) Kennicutt et al. (2008); (2) Skillman et al. (1989b); (3) Hodge & Miller (1995); (4) Hunter & Hoffman (1999); (5) Lee et al. (2005); (6) Webster & Smith (1983); (7) Aguero & Carranza (1985); (8) Stasińska et al. (1986); (9) Zaritsky et al. (1994); (10) Tüllmann et al. (2003); (11) Saviane et al. (2008); (12) Dalcanton et al. (2009); (13) Vila Costas & Edmunds (1993); (14) Skrutskie et al. (2003); (15) Dale et al. (2009); (16) Lee et al. (2010); (17) van Zee et al. (1997b); (18) van Zee et al. (1997a); (19) Russell & Dopita (1990); (20) Vermeij & van der Hulst (2002); (21) Pagel et al. (1979); (22) Christensen et al. (1997); (23) Kennicutt et al. (2003b); (24) Smith (1975); (25) Davidson & Kinman (1982); (26) Lee et al. (2003a); (27) Moustakas & Kennicutt (2006a); (28) van Zee & Haynes (2006); (29) Kewley et al. (2005); (30) McCall et al. (1985); (31) Vilchez et al. (1988b); (32) Bresolin et al. (1999); (33) Crockett et al. (2006); (34) Magrini et al. (2007); (35) Rosolowsky & Simon (2008); (36) Skillman et al. (2003); (37) Talent (1983); (38) Masegosa et al. (1991); (39) Ferguson et al. (1998); (40) van Zee et al. (1998); (41) Castellanos et al. (2002); (42) Miller (1996); (43) Hidalgo-Gómez & Olofsson (2002); (44) Hunter & Gallagher (1985); (45) Pagel et al. (1980); (46) Storch-Bergmann et al. (1994); (47) Walsh & Roy (1997); (48) Aguero & Paolantonio (1997); (49) Raimann et al. (2000); (50) Disney & Pottasch (1977); (51) Masegosa et al. (1994); (52) Loveday (1996); (53) Meurer et al. (1992); (54) Lee & Skillman (2004); (55) Hunter et al. (1982); (56) Kennicutt et al. (1980); (57) Gonzalez-Delgado et al. (1994); (58) Roy et al. (1996); (59) Martin (1997); (60) Buckalew et al. (2005); (61) Thuan & Izotov (2005); (62) Whiting et al. (2007); (63) Garnett et al. (1997); (64) Engelbracht et al. (2008); (65) Gil de Paz et al. (2000b); (66) Gil de Paz et al. (2000a); (67) Kniazev et al. (2004); (68) Izotov et al. (2006); (69) Lee et al. (2003b); (70) Croxall et al. (2009); (71) Skillman et al. (1989a); (72) Pustilnik et al. (2003); (73) Skillman et al. (1994); (74) Bresolin et al. (2005); (75) Moustakas & Kennicutt (2006b); (76) Miller & Hodge (1996); (77) Froebrich & Meusinger (2000); (78) Kinman & Hintzen (1981); (79) Hopp & Schulte-Ladbeck (1991); (80) Alloin et al. (1979); (81) Garnett & Shields (1987); (82) Pustilnik et al. (2005); (83) Johnson et al. (1997); (84) van Driel et al. (1998); (85) van Zee et al. (2006); (86) Moles et al. (1990); (87) Kniazev et al. (2005); (88) Magrini et al. (2005); (89) Lee et al. (2007); (90) Peña et al. (2007); (91) Adelman-McCarthy et al. (2008); (92) McCall et al. (1981); (93) Vilchez et al. (1988a); (94) Oey & Kennicutt (1993); (95) Dutil & Roy (2003); (96) Bresolin & Kennicutt (2002); (97) Gallagher et al. (2005); (98) French (1980); (99) Zamorano & Rego (1986); (100) De Robertis (1987); (101) Gonzalez-Riestra et al. (1988); (102) Guseva et al. (2000); (103) Gallagher & Hunter (1989); (104) Kobulnicky & Skillman (1996); (105) Kobulnicky et al. (1999); (106) Kniazev et al. (2003); (107) Matteucci & Tosi (1985); (108) Diaz et al. (2000); (109) Cedrés & Cepa (2002); (110) Izotov et al. (1997); (111) Pérez-Montero & Diaz (2003); (112) Shi et al. (2005); (113) Sabbadin et al. (1984); (114) van Zee (2000); (115) Gil de Paz et al. (2007); (116) Martin & Belley (1997); (117) Kennicutt & Skillman (2001); (118) Hidalgo-Gómez et al. (2001); (119) Ryder (1995); (120) Diaz et al. (1991); (121) Bresolin et al. (2004); (122) Garnett et al. (2004); (123) Vaduvescu et al. (2007); (124) Dufour et al. (1980); (125) Welch (1970); (126) Walsh & Roy (1989); (127) Kobulnicky et al. (1997); (128) López-Sánchez et al. (2007); (129) Liang et al. (2007); (130) Hawley (1978); (131) Rayo et al. (1982); (132) Skillman (1985); (133) Torres-Peimbert et al. (1989); (134) Garnett & Kennicutt (1994); (135) Kennicutt & Garnett (1996); (136) Kennicutt et al. (2003a); (137) Bresolin (2007); (138) Izotov et al. (2007); (139) Izotov et al. (1994); (140) Webster et al. (1983); (141) Skillman et al. (1997); (142) Chun (1983); (143) Edmunds & Pagel (1984)

NOTE. — The columns (left to right) are the galaxy name, right ascension as *hh:mm:ss.s*, declination as *dd:mm:ss*, coordinate reference, heliocentric redshift, distance, oxygen abundance and corresponding method and reference(s), and membership in the overlapping LVL and spectroscopic (IRS) subsamples.

^a The oxygen abundances drawn from the literature are based on either the 4363Å line, the strong line method, a mix of these two methods, or, in one case, a planetary nebula (PN) observation.

^b This velocity is erroneously listed as 869 instead of 1469 in Dale et al. (2009).

^c This oxygen abundance is believed to be affected by tidal interaction in the M81 group and unrepresentative of the galaxy (Croxall et al. 2009).

TABLE 2
SPECTROSCOPIC SAMPLE DATA.

Galaxy	IRS-Aperture-Matched Photometry ^a				Synthetic Photometry					$F_{8(S)}^{\text{afe,d,e}}$ (10^{-12} erg/s/cm ²)	$F_{\text{mir}(S)}^{\text{afe,d}}$ (10^{-12} erg/s/cm ²)
	$f_{3.6}$ (mJy)	$f_{4.5}$ (mJy)	$f_{5.8}$ (mJy)	f_8 (mJy)	$f_{24(S)}^b$ (mJy)	$f_8^{\text{str,c}}$ (mJy)	$f_{8(S)}^{\text{ent,d}}$ (mJy)	$f_{8(S)}^{\text{nl,d}}$ (mJy)	$f_{8(S)}^{\text{afe,d,e}}$ (mJy)		
MRK 0033	4.32E+1	3.19E+1	9.32E+1	2.48E+2	1.29 ± 0.02 E+3	1.08E+1	2.63 ± 0.167 E+1	5.16 ± 0.72 E+0	1.96 ± 0.029 E+2	3.01 ± 0.055 E+1	5.42 ± 0.061 E+1
NGC 0337	4.81E+1	3.37E+1	9.27E+1	2.26E+2	4.24 ± 0.07 E+2	1.17E+1	4.05 ± 0.184 E+1	2.10 ± 0.47 E+0	1.62 ± 0.028 E+2	2.42 ± 0.054 E+1	4.56 ± 0.056 E+1
NGC 0584	5.23E+2	3.13E+2	2.23E+2	1.36E+2	5.87 ± 0.10 E+1	1.31E+2	1.87 ± 0.216 E+1	0.19 ± 2.12 E-1	0.00 ± 1.200 E-1	0.00 ± 1.560 E-2	2.20 ± 0.453 E+0
NGC 0628	7.25E+1	4.70E+1	6.04E+1	1.15E+2	7.38 ± 0.12 E+1	1.72E+1	1.03 ± 0.020 E+1	2.02 ± 0.41 E+0	8.23 ± 0.112 E+1	1.26 ± 0.022 E+1	2.13 ± 0.024 E+1
NGC 1097	5.54E+2	3.88E+2	9.06E+2	2.27E+3	5.30 ± 0.08 E+3	1.38E+2	3.71 ± 0.020 E+2	2.19 ± 0.06 E+1	1.63 ± 0.003 E+3	2.46 ± 0.005 E+2	4.49 ± 0.006 E+2
NGC 1316	1.25E+3	7.70E+2	5.95E+2	4.17E+2	3.86 ± 0.06 E+2	3.08E+2	1.20 ± 0.028 E+2	1.44 ± 0.66 E+0	0.00 ± 4.890 E-1	0.00 ± 7.370 E-2	9.56 ± 0.716 E+0
NGC 1482	2.88E+2	2.15E+2	8.82E+2	2.47E+3	4.83 ± 0.08 E+3	7.71E+1	2.42 ± 0.045 E+2	1.37 ± 0.07 E+1	1.99 ± 0.004 E+3	2.99 ± 0.007 E+2	5.30 ± 0.011 E+2
NGC 1512	2.62E+2	1.66E+2	2.17E+2	4.07E+2	4.68 ± 0.07 E+2	6.43E+1	4.84 ± 0.361 E+1	5.77 ± 1.06 E+0	2.68 ± 0.052 E+2	4.04 ± 0.101 E+1	7.44 ± 0.105 E+1
NGC 1566	5.03E+2	3.63E+2	4.18E+2	7.06E+2	1.06 ± 0.02 E+3	1.24E+2	2.29 ± 0.029 E+2	6.11 ± 1.02 E+0	3.33 ± 0.040 E+2	5.15 ± 0.074 E+1	9.90 ± 0.083 E+1
NGC 2403	2.13E+2	1.42E+2	2.02E+2	3.71E+2	2.59 ± 0.04 E+2	5.12E+1	3.70 ± 0.174 E+1	5.56 ± 1.33 E+0	2.50 ± 0.041 E+2	3.76 ± 0.081 E+1	7.45 ± 0.080 E+1
NGC 2798	2.78E+2	2.07E+2	6.68E+2	1.86E+3	6.07 ± 0.10 E+3	7.13E+1	1.75 ± 0.020 E+2	1.80 ± 0.12 E+1	1.48 ± 0.004 E+3	2.25 ± 0.007 E+2	4.04 ± 0.008 E+2
NGC 2841	9.27E+2	5.38E+2	4.07E+2	2.77E+2	1.45 ± 0.02 E+2	2.30E+2	4.77 ± 0.222 E+1	1.56 ± 0.78 E+0	0.00 ± 1.070 E+0	0.00 ± 1.690 E-1	1.04 ± 0.097 E+1
NGC 2976	1.33E+2	8.92E+1	1.65E+2	3.37E+2	4.14 ± 0.06 E+2	3.21E+1	1.00 ± 0.038 E+2	3.85 ± 1.59 E+0	1.91 ± 0.059 E+2	2.86 ± 0.116 E+1	5.62 ± 0.130 E+1
NGC 3049	2.99E+1	2.13E+1	5.95E+1	1.58E+2	5.91 ± 0.09 E+2	7.46E+0	1.27 ± 0.161 E+1	2.69 ± 0.55 E+0	1.27 ± 0.023 E+2	1.92 ± 0.043 E+1	3.46 ± 0.049 E+1
NGC 3184	1.30E+2	8.73E+1	1.62E+2	3.69E+2	4.97 ± 0.08 E+2	3.17E+1	4.64 ± 0.383 E+1	1.02 ± 0.14 E+1	2.73 ± 0.064 E+2	4.19 ± 0.123 E+1	7.20 ± 0.146 E+1
NGC 3190	3.12E+2	1.92E+2	1.80E+2	2.30E+2	1.57 ± 0.03 E+2	7.95E+1	4.04 ± 0.189 E+1	1.99 ± 0.48 E+0	1.02 ± 0.026 E+2	1.56 ± 0.051 E+1	3.44 ± 0.065 E+1
NGC 3265	5.32E+1	3.59E+1	8.56E+1	2.22E+2	5.31 ± 0.09 E+2	1.32E+1	1.42 ± 0.246 E+1	2.47 ± 0.57 E+0	1.84 ± 0.035 E+2	2.79 ± 0.065 E+1	4.99 ± 0.075 E+1
NGC 3351	2.40E+2	1.57E+2	2.66E+2	5.85E+2	1.85 ± 0.03 E+3	5.92E+1	9.65 ± 0.158 E+1	1.02 ± 0.09 E+1	3.99 ± 0.025 E+2	5.97 ± 0.050 E+1	1.12 ± 0.005 E+2
NGC 3521	3.91E+2	2.51E+2	3.37E+2	6.44E+2	6.67 ± 0.10 E+2	9.66E+1	1.66 ± 0.018 E+2	5.18 ± 0.73 E+0	3.67 ± 0.026 E+2	5.43 ± 0.050 E+1	1.05 ± 0.006 E+2
NGC 3627	3.68E+2	2.33E+2	2.87E+2	5.08E+2	6.31 ± 0.10 E+2	9.16E+1	9.03 ± 0.183 E+1	5.03 ± 0.68 E+0	3.02 ± 0.022 E+2	4.61 ± 0.043 E+1	9.45 ± 0.059 E+1
NGC 3773	2.96E+1	2.06E+1	4.49E+1	1.04E+2	2.72 ± 0.04 E+2	7.14E+0	1.73 ± 0.111 E+1	4.89 ± 4.40 E-1	7.55 ± 0.285 E+1	1.15 ± 0.055 E+1	2.02 ± 0.063 E+1
NGC 4125	1.03E+3	6.13E+2	4.60E+2	2.90E+2	1.13 ± 0.02 E+2	2.55E+2	3.57 ± 0.276 E+1	9.88 ± 5.09 E-1	0.00 ± 1.900 E-1	0.00 ± 2.620 E-2	7.96 ± 1.040 E+0
NGC 4254	1.86E+2	1.26E+2	2.83E+2	7.13E+2	8.06 ± 0.13 E+2	4.63E+1	8.54 ± 0.161 E+1	6.01 ± 0.77 E+0	5.49 ± 0.027 E+2	8.23 ± 0.050 E+1	1.45 ± 0.005 E+2
NGC 4321	2.07E+2	1.41E+2	3.36E+2	8.57E+2	1.22 ± 0.02 E+3	5.05E+1	8.69 ± 0.050 E+1	9.63 ± 0.69 E+0	6.69 ± 0.022 E+2	1.01 ± 0.005 E+2	1.79 ± 0.004 E+2
NGC 4536	3.56E+2	2.55E+2	8.46E+2	2.25E+3	4.99 ± 0.08 E+3	8.94E+1	1.96 ± 0.018 E+2	1.80 ± 0.11 E+1	1.81 ± 0.003 E+3	2.73 ± 0.007 E+2	4.91 ± 0.007 E+2
NGC 4559	5.18E+1	3.45E+1	7.08E+1	1.56E+2	1.34 ± 0.02 E+2	1.26E+1	2.12 ± 0.152 E+1	1.70 ± 0.40 E+0	1.11 ± 0.021 E+2	1.69 ± 0.041 E+1	3.10 ± 0.043 E+1
NGC 4625	3.38E+1	2.20E+1	4.91E+1	1.19E+2	9.71 ± 0.16 E+1	8.35E+0	2.12 ± 0.189 E+1	5.64 ± 3.82 E-1	8.54 ± 0.251 E+1	1.27 ± 0.046 E+1	2.25 ± 0.055 E+1
NGC 4631	2.16E+2	1.56E+2	4.47E+2	1.08E+3	1.38 ± 0.02 E+3	5.53E+1	1.01 ± 0.006 E+2	4.83 ± 0.55 E+0	8.57 ± 0.018 E+2	1.30 ± 0.004 E+2	2.28 ± 0.004 E+2
NGC 4736	1.29E+3	8.28E+2	8.63E+2	1.24E+3	1.21 ± 0.02 E+3	3.19E+2	3.20 ± 0.027 E+2	4.66 ± 0.45 E+0	5.59 ± 0.028 E+2	8.59 ± 0.050 E+1	2.19 ± 0.008 E+2
NGC 4826	7.98E+2	5.21E+2	7.49E+2	1.52E+3	1.83 ± 0.03 E+3	1.98E+2	2.00 ± 0.037 E+2	1.17 ± 0.07 E+1	1.05 ± 0.004 E+3	1.59 ± 0.007 E+2	2.90 ± 0.011 E+2
NGC 5033	2.76E+2	1.84E+2	3.01E+2	6.46E+2	7.17 ± 0.11 E+2	6.88E+1	1.22 ± 0.032 E+2	1.62 ± 0.45 E+0	4.21 ± 0.034 E+2	6.34 ± 0.064 E+1	1.24 ± 0.008 E+2
NGC 5055	4.90E+2	3.10E+2	4.14E+2	7.91E+2	7.17 ± 0.11 E+2	1.23E+2	1.01 ± 0.004 E+2	6.39 ± 0.76 E+0	5.25 ± 0.022 E+2	7.98 ± 0.044 E+1	1.49 ± 0.004 E+2
NGC 5194	4.16E+2	2.71E+2	5.08E+2	1.16E+3	1.44 ± 0.02 E+3	1.02E+2	2.11 ± 0.008 E+2	1.51 ± 0.03 E+1	7.79 ± 0.009 E+2	1.18 ± 0.002 E+2	2.22 ± 0.002 E+2
NGC 5195	7.86E+2	5.20E+2	6.65E+2	1.15E+3	2.50 ± 0.04 E+3	1.95E+2	2.59 ± 0.052 E+2	1.17 ± 0.14 E+1	6.32 ± 0.056 E+2	9.74 ± 0.103 E+1	2.18 ± 0.012 E+2
NGC 5713	1.05E+2	7.61E+1	2.80E+2	7.83E+2	1.52 ± 0.02 E+3	2.57E+1	1.15 ± 0.025 E+2	4.54 ± 0.49 E+0	5.97 ± 0.024 E+2	8.96 ± 0.044 E+1	1.64 ± 0.007 E+2
NGC 5866	8.07E+2	5.14E+2	4.47E+2	4.72E+2	2.88 ± 0.05 E+2	2.01E+2	1.12 ± 0.034 E+2	2.76 ± 1.34 E+0	1.51 ± 0.043 E+2	2.23 ± 0.081 E+1	4.91 ± 0.097 E+1
NGC 6946	5.87E+2	4.38E+2	1.65E+3	4.29E+3	9.42 ± 0.15 E+3	1.39E+2	4.62 ± 0.082 E+2	3.79 ± 0.12 E+1	3.41 ± 0.007 E+3	5.19 ± 0.013 E+2	9.21 ± 0.022 E+2
NGC 7331	2.56E+2	1.57E+2	1.55E+2	2.03E+2	1.94 ± 0.03 E+2	6.43E+1	3.55 ± 0.108 E+1	1.86 ± 0.38 E+0	9.73 ± 0.139 E+1	1.48 ± 0.026 E+1	2.92 ± 0.029 E+1
NGC 7552	4.31E+2	3.87E+2	1.18E+3	3.13E+3	1.39 ± 0.02 E+4	1.09E+2	4.62 ± 0.040 E+2	3.67 ± 0.09 E+1	2.36 ± 0.004 E+3	3.58 ± 0.007 E+2	6.51 ± 0.012 E+2
NGC 7793	5.56E+1	3.66E+1	6.66E+1	1.40E+2	1.35 ± 0.02 E+2	1.31E+1	1.04 ± 0.071 E+1	3.11 ± 0.64 E+0	1.06 ± 0.017 E+2	1.71 ± 0.033 E+1	2.89 ± 0.034 E+1

NOTE. — The columns (left to right) are the galaxy name, IRS aperture matched flux density for the four IRAC channels, synthetic MIPS 24 μ m flux density obtained from the IRS spectroscopy, synthetic IRAC 8 μ m flux density for the fitted starlight, dust continuum, atomic and molecular line, and aromatic spectral contributions, and integrated fluxes for the aromatic features in both the 8 μ m complex and the mid-infrared ($5.5\mu\text{m} < \lambda < 20\mu\text{m}$). The compact format $X.XX \pm Y.YY$ EZ implies $(X.XX \pm Y.YY) \times 10^Z$.

^a One-sigma uncertainties of 10% were adopted for the IRS-aperture-matched photometry from comparison to synthetic spectrophotometry at 24 μ m.

^b The uncertainty quoted for the synthetic MIPS 24 μ m photometry is the standard deviation for 1000 measurements based on random realizations of the error in the IRS spectrum.

^c Because the stellar model is normalized at 3.6 μ m, the uncertainty in f_8^{str} is the same 10% described in footnote a.

^d The uncertainty represents the standard deviation in measurements derived from independent PAHFIT results for 1000 random realizations of the error in the IRS spectrum.

^e The five aromatic features at 7.42, 7.60, 7.85, 8.33, and 8.62 μ m (that fall entirely within the IRAC 8 μ m band) are included, but not the two (partially overlapping) features at 6.22 and 6.69 μ m.

TABLE 3 — *Continued*

Galaxy	f_8^a (mJy)	Synthetic Stellar Photometry ^b				f_8^{cnt} (mJy)	f_8^{afe} (mJy)	F_8^{afe} (10^{-12} erg/s/cm ²)	F_{TR} (10^{-12} erg/s/cm ²)
		$f_{4.5}^{\text{str}}$ (mJy)	$f_{5.8}^{\text{str}}$ (mJy)	f_8^{str} (mJy)	f_{24}^{str} (mJy)				
UGC 07719	1.22 ± 0.20 E+0	2.92E+0	1.71E+0	1.15 ± 0.16 E+0	1.35E-1	7.33 ± 7.93 E-2	0.00 ± 7.32 E-2	0.00 ± 1.12 E-2	1.31 ± 0.12 E+1
NGC 4631	5.85 ± 0.73 E+3	7.15E+2	4.88E+2	3.05 ± 0.43 E+2	3.57E+1	9.78 ± 3.80 E+2	4.28 ± 0.35 E+3	6.55 ± 0.54 E+2	1.30 ± 0.12 E+4
NGC 4656	1.02 ± 0.13 E+2	5.86E+1	3.83E+1	2.23 ± 0.30 E+1	2.57E+0	1.46 ± 0.66 E+1	6.10 ± 0.61 E+1	9.34 ± 0.94 E+0	7.25 ± 0.63 E+2
UGC 07950	4.33 ± 0.57 E+0	6.48E+0	4.34E+0	2.62 ± 0.36 E+0	3.03E-1	1.06 ± 0.28 E+0	6.04 ± 2.60 E-1	9.24 ± 3.98 E-2	2.31 ± 0.22 E+1
UGC 07916	1.90 ± 0.28 E+0	2.57E+0	1.71E+0	1.01 ± 0.14 E+0	1.18E-1	3.32 ± 1.23 E-1	5.26 ± 1.14 E-1	8.05 ± 1.75 E-2	1.03 ± 0.11 E+1
NGC 4736	4.82 ± 0.64 E+3	2.03E+3	1.37E+3	8.52 ± 1.20 E+2	9.85E+1	7.71 ± 3.13 E+2	3.00 ± 0.29 E+3	4.59 ± 0.44 E+2	8.60 ± 0.78 E+3
NGC 4826	2.24 ± 0.29 E+3	1.42E+3	9.58E+2	5.97 ± 0.85 E+2	6.90E+1	3.83 ± 1.46 E+2	1.18 ± 0.13 E+3	1.81 ± 0.21 E+2	4.43 ± 0.41 E+3
UGCA 320	3.42 ± 0.44 E+0	1.11E+1	3.23E+0	3.42 ± 0.46 E+0	5.09E-1	7.83 ± 2.22 E-1	0.00 ± 2.05 E-1	0.00 ± 3.14 E-2	3.40 ± 0.31 E+1
UGC 08188	3.56 ± 0.45 E+1	3.72E+1	2.52E+1	1.52 ± 0.21 E+1	1.80E+0	7.97 ± 2.32 E+0	1.16 ± 0.21 E+1	1.78 ± 0.33 E+0	1.37 ± 0.13 E+2
MCG -03-34-002	2.90 ± 0.39 E+0	4.68E+0	3.22E+0	1.97 ± 0.27 E+0	2.39E-1	4.40 ± 1.89 E-1	4.55 ± 1.74 E-1	6.96 ± 2.67 E-2	7.86 ± 0.84 E+0
CGCG 217-018	4.71 ± 0.61 E+0	4.23E+0	2.86E+0	1.72 ± 0.23 E+0	2.05E-1	4.44 ± 3.06 E-1	2.39 ± 0.28 E+0	3.66 ± 0.43 E-1	1.28 ± 0.12 E+1
UGC 08313	7.12 ± 0.91 E+0	5.89E+0	4.16E+0	2.55 ± 0.35 E+0	3.11E-1	5.91 ± 4.63 E-1	3.73 ± 0.43 E+0	5.70 ± 0.65 E-1	2.26 ± 0.20 E+1
UGC 08320	7.09 ± 0.93 E+0	1.20E+1	5.34E+0	4.83 ± 0.65 E+0	5.58E-1	9.85 ± 4.61 E-1	1.19 ± 0.43 E+0	1.83 ± 0.65 E-1	4.16 ± 0.41 E+1
NGC 5195	6.46 ± 0.81 E+2	4.95E+2	3.35E+2	2.07 ± 0.28 E+2	2.40E+1	6.31 ± 4.20 E+1	3.52 ± 0.39 E+2	5.39 ± 0.59 E+1	9.40 ± 0.72 E+2
ESO 444-G084	7.40 ± 1.50 E-1	2.13E+0	1.46E+0	7.40 ± 1.01 E-1	1.03E-1	1.56 ± 0.48 E-1	0.00 ± 4.44 E-2	0.00 ± 6.80 E-3	4.33 ± 0.67 E+0
UGC 08638	2.24 ± 0.33 E+0	4.94E+0	2.74E+0	2.03 ± 0.28 E+0	2.49E-1	0.45 ± 1.46 E-1	1.58 ± 1.34 E-1	2.42 ± 2.06 E-2	1.23 ± 0.14 E+1
NGC 5264	4.21 ± 0.53 E+1	3.09E+1	2.04E+1	1.23 ± 0.17 E+1	1.39E+0	9.71 ± 2.74 E+0	1.89 ± 0.25 E+1	2.89 ± 0.39 E+0	8.84 ± 0.91 E+1
UGC 08837	1.07 ± 0.14 E+1	9.96E+0	6.59E+0	3.83 ± 0.52 E+0	4.56E-1	4.77 ± 6.93 E-1	5.95 ± 0.64 E+0	9.11 ± 0.98 E-1	3.29 ± 0.35 E+1
KKH 086	<1.38E+0	7.20E-1	5.54E-1	3.22 ± 0.45 E-1	3.89E-2	<2.21E-1	<7.85E-1	<1.20E-1	<8.95E+0
[KK98] 230	<7.60E-1	2.99E-1	1.99E-1	1.16 ± 0.15 E-1	1.40E-2	<1.54E-1	<4.59E-1	<7.03E-2	<4.95E+0
NGC 5585	8.86 ± 1.11 E+1	5.21E+1	3.45E+1	2.06 ± 0.28 E+1	2.36E+0	1.60 ± 0.58 E+1	4.87 ± 0.53 E+1	7.45 ± 0.81 E+0	3.17 ± 0.33 E+2
UGC 09240	7.79 ± 1.00 E+0	9.50E+0	6.23E+0	3.63 ± 0.49 E+0	4.20E-1	1.01 ± 0.51 E+0	2.95 ± 0.47 E+0	4.51 ± 0.72 E-1	2.90 ± 0.27 E+1
NGC 5949	1.50 ± 0.19 E+2	4.22E+1	2.83E+1	1.71 ± 0.23 E+1	1.97E+0	2.78 ± 0.97 E+1	9.81 ± 0.90 E+1	1.50 ± 0.14 E+1	2.57 ± 0.26 E+2
ESO 347-G017	2.94 ± 0.41 E+0	5.57E+0	3.21E+0	2.19 ± 0.30 E+0	2.60E-1	0.66 ± 1.91 E-1	6.36 ± 1.76 E-1	9.73 ± 2.70 E-2	1.81 ± 0.18 E+1
NGC 4163	5.64 ± 0.74 E+0	1.04E+1	6.69E+0	3.83 ± 0.52 E+0	4.34E-1	6.81 ± 3.67 E-1	1.06 ± 0.34 E+0	1.62 ± 0.52 E-1	1.43 ± 0.16 E+1

NOTE. — The columns (left to right) are the galaxy name, IRAC $8\mu\text{m}$ flux density, modelled synthetic IRAC 4.5, 5.8 and $8\mu\text{m}$ and MIPS $24\mu\text{m}$ stellar photometry, computed dust continuum and $8\mu\text{m}$ aromatic feature complex contributions to the IRAC $8\mu\text{m}$ band, integrated aromatic emission for the $8\mu\text{m}$ complex, and the total infrared flux between $3\mu\text{m}$ and $1100\mu\text{m}$. The compact format $X.XX \pm Y.YY \text{EZ}$ implies $(X.XX \pm Y.YY) \times 10^Z$.

^a Photometry for the other *Spitzer* bands can be found in the LVL survey description and infrared photometry paper (Dale et al. 2009).

^b The uncertainties in the synthetic stellar photometry are the propagated uncertainties in the IRAC $3.6\mu\text{m}$ photometry, thus the uncertainty in f_X^{str} is simply the provided uncertainty in f_8^{str} multiplied by the ratio of $f_X^{\text{str}}/f_8^{\text{str}}$.

^c The NGC 1800 entry is the combined photometry of that galaxy and MCG -05-13-004 (which spatially overlap).